Condensed phase electron transfer beyond the Condon approximation

Condensed phase electron transfer beyond the Condon approximation

Michael G. Mavros, Diptarka Hait, and Troy Van Voorhis*

Department of Chemistry, Massachusetts Institute of Technology, 77 Massachusetts Ave, Cambridge MA 02139

Condensed phase electron transfer problems are often simplified by making the Condon approximation: the approximation that the coupling connecting two charge-transfer diabatic states is a constant. Unfortunately, the Condon approximation does not predict the existence of conical intersections, which are ubiquitous in both gas-phase and condensed-phase photochemical dynamics. In this paper, we develop a formalism to treat condensed-phase dynamics beyond the Condon approximation. We show that even for an extremely simple test system, hexaaquairon(II) / hexaaquairon(III) self-exchange in water, the electronic coupling is expected to fluctuate rapidly and non-Condon effects must be considered to obtain quantitatively accurate ultrafast nonequilibrium dynamics. As diabatic couplings are expected to fluctuate substantially in many condensed-phase electron transfer systems, non-Condon effects may be essential to quantitatively capture accurate short-time dynamics.

I. INTRODUCTION

Electron transfer is a fundamental process in chemistry and biology. An exact dynamical description of this process from first principles is difficult if not impossible due to the multitude of degrees of freedom involved in solvent reorganization. These solvent degrees of freedom are critical for properly describing electron transfer rates and dynamics, as observed originally by Marcus [1–3] and subsequently reinforced by many others [4–12]. Because exact quantum methods cannot describe systems with thousands of degrees of freedom without running into exponential scaling, approximate models are often invoked to describe electron transfer dynamics.

One important model for describing condensed-phase electron transfer is the spin-boson model, a system-bath model that describes a two-level system coupled linearly to a large number of harmonic bath modes [13]. While simpler than an atomistic model, the spin-boson model still cannot be solved analytically for a general bath: the exact density matrix and the propagator must each be expanded in the basis of a many-dimensional collection of harmonic oscillators, again leading to exponential scaling.

For certain classes of baths, it is possible to converge the dynamics on to the numerically-exact result before reaching the point where exponential scaling becomes prohibitive. To enumerate a few: the QUAPI method [14–19] will converge so long as the bath autocorrelation function decays quickly as $t \to \infty$; the MCTDH method [20, 21] will converge so long as the majority of the bath is slow with respect to population transfer and can thus be treated classically or semi-classically; and the HEOM method [22, 23] will converge if the bath can be accurately represented with a Debye spectral density. The treatment of a general bath is largely limited to more approximate methods, a few of which are detailed in Refs. [24–26].

The spin-boson model is useful; however, it is not without its limitations. One limitation is that the spin-boson model makes the Condon approximation—which states that electronic transitions occur instantaneously on the timescale of nuclear motion, or alternatively that the electronic coupling operator $\hat{V}$ is a constant that does not depend on nuclear coordinates [27]. This approximation is often successful, but in certain cases—specifically, in cases with ultrafast electronic relaxation through conical intersections—it is demonstrably bad.

Optically-excited molecules can relax back to the ground state either through radiative processes or non-radiative processes. When relaxation is fast, it is nearly always the case that molecules relax from excited state to ground state through *conical intersections*—regions where the excited state adiabatic potential energy surface cross the ground state adiabatic potential energy surface [28, 29]. Conical intersections have been studied extensively in the gas phase both theoretically [30–35] and experimentally [36–38]. Condensed-phase photochemistry is often much more complicated, as a continuum of bath modes must now be considered. Especially challenging to incorporate are low-frequency solvent modes, which can play a role in the dynamics even though passage through conical intersections is rapid.

Condensed-phase conical intersections are less studied, though there have been several important experimental and theoretical achievements in their description over the last two decades. While some early experiments observed conical intersections in small molecules such as pyridine [39], interest in understanding condensed-phase conical intersections has grown due to an increasing desire to understand the isomerization of biomolecules, including biofluorophores [40], DNA/RNA [36, 41], and retinal [42–44]. Computational and theoretical models have been of utmost importance in interpreting experimental data. For example, Martinez et al have described conical intersections in biofluorophores using high-level electronic structure calculations in QM/MM dynamics [45, 46]. Additionally, Burghardt, Hynes et al have successfully described the conical intersection in retinal (and other Schiff bases) by parameterizing a model

* tvan@mit.edu

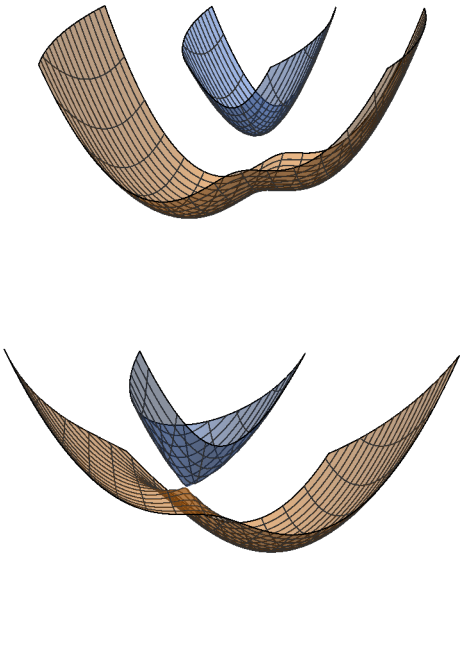

(a)

(b)

Figure 1. Conical intersections in N dimensions manifest themselves as surfaces intersecting along N-2 dimensions; thus, the smallest dimension along which two adiabats can intersect is two, and in 2D that intersection is a point. (a) Under the Condon approximation, the coupling can *never* be zero for any value of the two nuclear coordinates, and the two adiabats will *never* intersect; the closest they get to each other is an avoided crossing, with magnitude $2V$. (b) If the coupling is allowed a linear dependence on each coordinate, the adiabats can intersect at a single point—a conical intersection.

diabatic Hamiltonian (which can then be diagonalized) along a choice of two relevant solvent degrees of freedom [47–50].

Despite these advancements, there is certainly room for the investigation of other models which incorporate non-Condon effects in order to develop a more complete picture of passage through conical intersections. In addition to some of the applications above, conical intersections in condensed phases are thought to be important for such processes as internal conversion and intersystem crossing [51], the understanding of which is essential for the prediction of quantum yields in devices such as photovoltaics and light-emitting diodes [52]—applications which may benefit greatly from a general model. Any progress towards the creation of such a model is thus of great scientific importance.

In order for a conical intersection to exist, two conditions must be upheld: (1) the excited state and ground state have the same energy; and (2) the electronic coupling between the two states must be zero [28]. Under the Condon approximation, the electronic coupling is not a function of the nuclear coordinates and can never be zero; thus, any model utilizing the Condon approximation, including the canonical spin-boson Hamiltonian, cannot describe conical intersections—phenomena which are paramount to the accurate description of photochemical processes. The qualitative difference is shown in Figure 1.

In this paper, we examine approximate solutions to the linear vibronic coupling Hamiltonian, which is an extension of the spin-boson Hamiltonian that includes these non-Condon effects. Using a generalized master equation formalism [53], we derive memory kernels for the linear vibronic coupling Hamiltonian to fourth order in perturbation theory in the electronic coupling, amounting to augmenting the well-studied second- and fourth-order kernels [20, 26, 54] with several extra non-Condon terms. In order to demonstrate the impact of these non-Condon terms, we examine the dynamics of the electron transfer self-exchange reaction Fe(II) + Fe(III)→Fe(III) + Fe(II) in water. We choose this system because (1) the partitioning between system and bath is straightforward; (2) the system is very well-studied [55–64]; and (3) there is no intrinsic bias driving the reaction one way or the other, meaning we are not in a regime where second-order methods are known to give qualitatively incorrect answers [20, 26].

II. THEORY

A. Spin-Boson Hamiltonian

Mathematically, the spin-boson model can be described with the Hamiltonian

$$\begin{aligned}\hat{H}_{SBM} &= \hat{H}_s + \hat{H}_b + \hat{H}_{s-b} \\ &= \begin{pmatrix} -\frac{\epsilon}{2} & V_0 \\ V_0 & \frac{\epsilon}{2} \end{pmatrix} + \sum_j \begin{pmatrix} \frac{\hat{p}_j^2}{2} + \frac{1}{2}\omega_j^2 \hat{x}_j^2 & 0 \\ 0 & \frac{\hat{p}_j^2}{2} + \frac{1}{2}\omega_j^2 \hat{x}_j^2 \end{pmatrix} \\ &\quad + \sum_j \begin{pmatrix} c_j \hat{x}_j & 0 \\ 0 & -c_j \hat{x}_j \end{pmatrix} \end{aligned} \tag{1}$$

where $\hat{H}_s$ is the Hamiltonian describing the two-level system, $\hat{H}_b$ the harmonic bath, and $\hat{H}_{s-b}$ the system-bath coupling. The two system states intrinsically differ in energy by a bias of ϵ and are coupled with a constant coupling V_0. The bath is comprised of a collection of harmonic oscillators with frequency ω_j that couple to the system with coupling c_j. The mass-scaled normal mode coordinates and momenta of the bath are represented by $\hat{x}_j$ and $\hat{p}_j$, respectively.

B. Linear Vibronic Coupling Hamiltonian

The most straightforward way to generalize the spin-boson Hamiltonian to include non-Condon effects is to add to the Hamiltonian a linear off-diagonal coupling to the bath. This new Hamiltonian is known as the *linear vibronic coupling* Hamiltonian, and has been studied in some detail [35, 65–70]

$$\hat{H}_{LVC} = \hat{H}_{SBM} + \sum_j \begin{pmatrix} 0 & V_j\hat{x}_j \\ V_j\hat{x}_j & 0 \end{pmatrix} \quad (2)$$

where $\hat{H}_{SBM}$ is the Hamiltonian defined in equation 1. This Hamiltonian has the advantage over $\hat{H}_{SBM}$ in that for some set of bath coordinates $\{\hat{x}_j\}$, it is possible for $\hat{H}_{LVC}$ to become proportional to the identity, allowing for the existence of conical intersections.

The linear vibronic coupling model can be understood by considering a two-level system interaction with a collection of harmonic oscillators. The two states have an energy difference, ϵ, and a coupling, V, which each fluctuate in time. The fluctuations in ϵ and V are driven by the action of the harmonic bath: some bath modes couple to the energy gap $\epsilon(t)$, driving its fluctuations; other bath modes couple to the coupling, $V(t)$, driving its fluctuations. In general, some bath modes could drive fluctuations in both ϵ and V, introducing cross-terms into the dynamics correlating the energy gap and coupling trajectories; as discussed in more detail in the next section, we have theoretical reasons to believe that the latter effects will be small in general, and we will be testing this hypothesis for a sample system.

C. Mode Continua in Condensed Phases

In the gas phase, the number of bath modes defining $\hat{H}_{SBM}$ or $\hat{H}_{LVC}$ is denumerable: a nonlinear molecule with N atoms has $3N-6$ vibrational models. In the condensed phase, where thousands of atoms must often be considered to get even a rudimentary description of charge-transfer dynamics, the number of bath modes quickly becomes innumerable. This facilitates the introduction of the *spectral density*, which coarse-grains an uncountably large number of bath modes in the condensed phase into a continuous function describing how strongly the bath couples to the diagonal elements of the system Hamiltonian at various frequencies ω[27]

$$J_{EG}(\omega) \equiv \frac{\pi}{2}\sum_j \frac{c_j^2}{\omega_j}\delta(\omega-\omega_j) \quad (3)$$

In the case of the linear vibronic coupling model, the bath also couples to the off-diagonal elements of the system Hamiltonian. We thus must introduce two more spectral densities: one describing the explicit coupling of the bath to off-diagonal elements of the Hamiltonian,

$$J_V(\omega) \equiv \frac{\pi}{2}\sum_j \frac{V_j^2}{\omega_j}\delta(\omega-\omega_j) \quad (4)$$

and one describing the cross-correlation between time-domain energy gap fluctuations and coupling fluctuations,

$$J_{cross}(\omega) \equiv \frac{\pi}{2}\sum_j \frac{c_j V_j}{\omega_j}\delta(\omega-\omega_j) \quad (5)$$

where ω_j, c_j, and V_j are Hamiltonian parameters introduced in equations 1 and 2. The details of how these spectral densities may be obtained from molecular simulation will be discussed in the following section.

For many physical systems, it is appropriate to make the approximation

$$J_{cross}(\omega) \approx 0$$

i.e., there is no correlation between bath modes which drive fluctuations in the energy gap and those which drive fluctuations in the coupling. While such a cross-coupling may exist in principle, in the vast majority of physical situations, very different bath motions are required to drive charge transfer in molecular systems like transition metal complexes and organic semiconductors. We call this approximation the "zero cross-correlation" (ZCC) approximation. We will later justify this approximation for the system which we have chosen to benchmark the dynamics method outlined in this paper, both through rigorous theoretical arguments and numerical results.

D. Generalized Master Equations and Memory Kernels

In order to study the dynamics generated by the linear vibronic coupling Hamiltonian, we have adopted a generalized master equation formalism [71–73], following the approach of Sparpaglione and Mukamel [53]. Generalized master equations are convenient ways of expressing the population dynamics of a system coupled to a bath when one is not interested in the detailed dynamics of the bath. For the correct choice of memory kernels, they are formally exact.

We will examine two particular choices of initial condition in this manuscript. The electron transfer system is comprised of two states, $|1\rangle$ and $|2\rangle$, corresponding to the reactant diabat and product diabat of a redox reaction, respectively. The first, dubbed the 'thermal' initial condition, refers to dynamics that begin on state $|1\rangle$ when the bath is in thermal equilibrium with state $|1\rangle$, which corresponds to non-driven electron transfer in solution.

The second, dubbed the 'nonequilibrium' initial condition, refers to dynamics that begin on state $|2\rangle$ when the bath is in thermal equilibrium with state $|1\rangle$, which corresponds to an instantaneous vertical transition from the equilibrium geometry of the reactant diabat to a high-energy point on the product diabat. This initial condition is similar to the initial condition in an optical experiment, as discussed in detail in Ref. [49]. While the non-equilibrium configuration draws its inspiration

from optical experiments, it should be noted that in the model iron(II)-iron(III) system we will study below, it would be very difficult (if not impossible) to prepare this initial state experimentally. Thus, the connection to an optical experiment should be thought of as no more than an analogy below. By design, the nonequilibrium initial condition will differ from the thermal one primarily at short times, ultimately allowing us to examine the influence of conical intersections on short-time versus long-time dynamics.

Both initial conditions are discussed in further detail in Appendix A. We note that we are probing the forward electron transfer reaction and the backward electron transfer reaction, respectively, when studying dynamics using the thermal initial condition and the nonequilibrium initial condition.

We now assume a set of generalized master equations of the form

$$\begin{aligned}\dot{p}_1 &= -\int_0^t K_1(t,t_1)p_1(t_1)dt_1 + \int_0^t K_2(t,t_1)p_2(t_1)dt_1 \\ \dot{p}_2 &= \int_0^t K_1(t,t_1)p_1(t_1)dt_1 - \int_0^t K_2(t,t_1)p_2(t_1)dt_1 \end{aligned} \quad (6)$$

Here, $p_1(t)$ and $p_2(t)$ are the populations of state $|1\rangle$ and state $|2\rangle$ respectively, and $K_1(t,t_1)$ and $K_2(t,t_1)$ are memory kernels describing the $1 \rightarrow 2$ and $2 \rightarrow 1$ population transfer process, respectively. These equations are similar to the equations in the Sparpaglione-Mukamel formalism [53], except that the kernels are no longer time-translationally invariant. This broken symmetry allows us to describe in general both thermal and nonequilibrium dynamics, as time translational symmetry is lost upon invoking the nonequilibrium initial condition. We emphasize that these generalized master equations are formally exact: one only has to determine the memory kernels in order to uniquely determine the populations of a two-level system. If the memory kernels are known exactly, solving these master equations will uniquely determine the populations exactly, as well. Other authors have recently applied this formalism to study chemical dynamics [74].

While determining $K(t,t_1)$ is tantamount to solving the time-dependent Schrödinger equation and is thus exponentially hard, one can expand $K(t,t_1)$ in a formal power series in the electronic coupling operator $\hat{V}$,

$$K(t,t_1) = \hat{V}^2 K^{(2)}(t,t_1) + \hat{V}^4 K^{(4)}(t,t_1) + ... \quad (7)$$

and use time-dependent perturbation theory in order to derive analytic expressions for $K^{(2)}$, $K^{(4)}$, and in principle all higher order terms. The exact kernel can then be reconstructed via a resummation technique, e.g. a Padé resummation [54, 75–77]. Note that truncating this perturbation series to second order for the spin-boson model results in the famous non-interacting blip approximation (NIBA) [24, 78], which is the Fermi's Golden Rule result for this problem—in many senses, it is a dynamical generalization of Marcus theory.

Using time-dependent perturbation theory and the master equations defined in equation 6, we have derived the non-Condon version of the memory kernel $K^{(2)}(t,t_1)$, giving us a version of NIBA which includes linear vibronic coupling and allowing us to compute generalized Marcus rates (and short-time dynamics!) beyond the Condon approximation. As we are ultimately interested in describing photochemistry, we present here memory kernels derived using the nonequilibrium initial condition: $p_2(0) = 1$ but the bath is initially in equilibrium with state $|1\rangle$. A full derivation of both the nonequilibrium kernels described in this paragraph as well as the memory kernels used for the thermal initial condition are presented in Appendix A. In summary, to second order in perturbation theory in $\hat{V}$,

$$K^{(2)}(t,t_1) = K_c^{(2)}(t,t_1) + K_{nc}^{(2)}(t,t_1) \quad (8)$$

where $K_c^{(2)}(t,t_1)$ is the Condon kernel,

$$K_c^{(2)}(t,t_1) = 2\langle V^2\rangle \exp\left[-Q'(t-t_1)\right]\cos\left(\phi(t,t_1) \pm \epsilon(t-t_1)\right) \quad (9)$$

defining

$$\phi(t,t_1) \equiv Q''(t-t_1) - 2Q''(t) + 2Q''(t_1) \quad (10)$$

$$\begin{aligned} Q'(t) &\equiv \frac{4}{\pi}\int_0^\infty d\omega \frac{J_{EG}(\omega)}{\omega^2}\left(1-\cos(\omega t)\right)\coth\left(\frac{\beta\omega}{2}\right) \\ Q''(t) &\equiv \frac{4}{\pi}\int_0^\infty d\omega \frac{J_{EG}(\omega)}{\omega^2}\sin(\omega t) \end{aligned} \quad (11)$$

and $K_{nc}^{(2)}(t,t_1)$ is the non-Condon kernel,

$$K_{nc}^{(2)}(t,t_1) = 2\exp\left[-Q'(t)\right]\left[S'(t-t_1)\cos\left(\phi(t,t_1)\pm\epsilon(t-t_1)\right) - S''(t-t_1)\sin\left(\phi(t,t_1)\pm\epsilon(t-t_1)\right)\right.$$
$$\left(\left(R'(t-t_1)-2R'(t)\right)\left(R'(t-t_1)-2R'(t_1)\right)-R''(t-t_1)^2\right)\cos\left(\phi(t,t_1)\pm\epsilon(t-t_1)\right)$$
$$+\left(2\left(R'(t)+R'(t_1)-R'(t-t_1)\right)R''(t-t_1)\right)\sin\left(\phi(t,t_1)\pm\epsilon(t-t_1)\right)$$
$$\pm 2V_0\left(R'(t)+R'(t_1)-R'(t-t_1)\right)\cos\left(\phi(t,t_1)\pm\epsilon(t-t_1)\right)$$
$$\left.\pm 2V_0 R''(t-t_1)\sin\left(\phi(t,t_1)\pm\epsilon(t-t_1)\right)\right] \quad (12)$$

defining

$$R'(t) \equiv \frac{2}{\pi}\int_0^\infty d\omega \frac{J_{cross}(\omega)}{\omega}\cos(\omega t)$$
$$R''(t) \equiv \frac{2}{\pi}\int_0^\infty d\omega \frac{J_{cross}(\omega)}{\omega}\coth\left(\frac{\beta\omega}{2}\right)\sin(\omega t) \quad (13)$$

and

$$S'(t) \equiv \frac{1}{\pi}\int_0^\infty d\omega J_V(\omega)\cos(\omega t)\coth\left(\frac{\beta\omega}{2}\right)$$
$$S''(t) \equiv \frac{1}{\pi}\int_0^\infty d\omega J_V(\omega)\sin(\omega t) \quad (14)$$

If we approximately neglect cross-correlation, $R'(t) = R''(t) = 0$, and Equation 12 simplifies:

$$K_{nc}^{(2)}(t,t_1) \approx 2\exp\left[-Q'(t)\right]\times \quad (15)$$
$$\left[S'(t-t_1)\cos\left(\phi(t,t_1)\pm\epsilon(t-t_1)\right)\right.$$
$$\left.-S''(t-t_1)\sin\left(\phi(t,t_1)\pm\epsilon(t-t_1)\right)\right]$$

Other authors have arrived at similar expressions [79–82]. In this manuscript, we will illustrate the utility of our formalism as well as assess the validity of the ZCC approximation for a relevant chemical problem. We would like to note in particular that in this regime and at short times, non-Condon effects only affect the pre-exponential piece of the Condon kernel—effectively modulating the coupling. This can be seen explicitly in Equations A15 and A16 in Appendix A.

Whether these non-Condon terms are expected to speed up or slow down electron transfer depends critically on how one defines the Condon rate in a system where the coupling fluctuates. If we take the average coupling in Equation 9 to be a root-mean-square average coupling, the effective coupling created by non-Condon effects at short times is strictly smaller than the Condon coupling. This observation implies that in this regime, non-Condon effects are expected to strictly *slow down* population transfer from $|1\rangle$ to $|2\rangle$. Other authors [80, 83, 84] have observed that averaging over the bath in a different manner (which amounts to rewriting Equation 9 in terms of $\langle V\rangle^2$) amounts to a strict non-Condon *speedup* in initial population transfer. Because the phase of the coupling is arbitrary, determining $\langle V\rangle$ from simulation is actually quite difficult. As such, we have chosen to define the Condon rate in terms of $\langle V^2\rangle$, a quantity much more readily obtainable.

We also note that *diabatic* population transfer is slowed down by non-Condon effects. In the Marcus normal regime, *adiabatic* population transfer is thus *sped up*, which makes sense: non-Condon effects facilitate traversal through conical intersections, a fast nonradiative decay pathway. To summarize, at short times, we find that non-Condon effects are expected to (1) slow down *diabatic* population transfer, but (2) speed up *adiabatic* population transfer if the experimentally-measurable coupling is taken to be the root-mean-square average coupling.

III. COMPUTATIONAL DETAILS

A. Extracting spectral densities from molecular simulation

Following our discussion in Section II D, it is apparent that in order to map chemical dynamics on to the spin-boson model, we require a way to extract the bath spectral density (or densities) from molecular simulation. Many authors [27, 59, 85, 86] have observed that the energy gap spectral density J_{EG} defined in equation 3 is related to the Fourier transform of the energy gap fluctuation autocorrelation function:

$$J_{EG}(\omega) = \frac{\beta\omega}{4}\int_0^\infty \langle\delta\Delta E(t)\delta\Delta E(0)\rangle\cos(\omega t)\,dt \quad (16)$$

where β is the inverse temperature, $\delta\Delta E(t) \equiv \Delta E(t) - \langle\Delta E\rangle$, and $\Delta E(t)$ is the energy gap, $\Delta E(t) \equiv E_2(t) - E_1(t)$. We recognize that the coupling and cross spectral densities defined in equations 4 and 5 can be written in terms of the coupling autocorrelation function and the energy gap - coupling cross correlation function, respectively:

$$J_V(\omega) = \beta\omega\int_0^\infty \langle\delta V(t)\delta V(0)\rangle\cos(\omega t)\,dt \quad (17)$$

$$J_{cross}(\omega) = \frac{\beta\omega}{2}\int_0^\infty \langle\delta\Delta E(t)\delta V(0)\rangle\cos(\omega t)\,dt \quad (18)$$

where $\delta V(t) \equiv V(t) - \langle V \rangle$.

Using these relations, we are able to map time correlation functions, quantities which we can readily extract from molecular simulation, on to the linear vibronic coupling Hamiltonian—a Hamiltonian with an in-principle numerically exact dynamical solution. In the remainder of this section, we discuss in detail how we extract the relevant information from simulation for a simple molecular system. In the following sections, we discuss the short-time and long-time dynamics which result from this mapping.

B. Simulation details

1. *Molecular dynamics simulations*

In order to examine the non-Condon effects on electron transfer dynamics predicted by equation 12, we have examined the aqueous electron transfer self-exchange reaction

$$Fe^{II} + Fe^{III} \rightarrow Fe^{III} + Fe^{II}$$

All molecular dynamics simulations were performed using the GROMACS 4.6.5 software package [87]. Two iron atoms (van der Waals parameters σ_i = 2.2 Å, ϵ_i = 0.0323 kcal/mol employing combination rule $\sigma_{ij} = \sqrt{\sigma_i \sigma_j}$ for both σ and ϵ [60]) were placed at their touching-sphere distance of 5.5 Å inside a periodic simulation box of dimensions 4 nm x 4.55 nm x 4.018 nm and then solvated with 2466 molecules of TIP3P water [88]. Iron atoms were allowed to interact with solvent via nonbonding interactions only. For NVT runs, the simulation box was coupled to a Nose-Hoover thermostat at 300 K with a time constant of 200 fs. Electrostatics were treated with the Particle Mesh Ewald method [89] with a cutoff of 1.5 nm; van der Waals interactions were cut off after 1.4 nm. A harmonic restraining potential ($r_0 = 0.35$ nm, $k = 100.0$ kJ mol^{-1} nm^{-2}) was used in order to keep the two irons in close proximity to each other.

A 1 ns NVT equilibration run was performed followed by a 1 ns NVT production run, each with a timestep of 1 fs. 300 configurations were sampled randomly from the production run at intervals of 100 fs; from each of these starting configurations, a 50 ps NVE run with a timestep of 0.5 fs was performed in order to ensure that correlation functions were sampled in the correct ensemble. For the NVE runs, Coulomb interactions were treated with the Reaction Field Zero method [90] with a cutoff of 1.3 nm, for better energy conservation; van der Waals interactions were treated as before.

For each snapshot in each NVE simulation, the energy was computed twice: once with the original force field and again with the charges on the two iron atoms swapped. The difference between these two energies is the energy gap, ΔE. The mean energy gap was subtracted from each data point to give fluctuations in the energy gap, $\delta\Delta E$. A 5 ps energy gap - energy gap time correlation function was computed using a shifting average over the data from each NVE run to give $\langle \delta\Delta E(t)\delta\Delta E(0)\rangle_{NVE}$; these correlation functions were then averaged over the 300 different NVE runs to give a the final energy gap - energy gap time correlation function at 300 K, $\langle \delta\Delta E(t)\delta\Delta E(0)\rangle_{NVE}$.

For these same snapshots, we also computed the coupling V using the *ansatz* outlined in the subsequent section. The mean coupling $\langle V \rangle$ was subtracted out from each value of $V(t)$ to give fluctuations in the coupling, δV. A 5 ps coupling - coupling time correlation function was computed in the same manner as for the energy gap correlation function (including the same averaging over many NVE trajectories) to give $\langle \delta V(t)\delta V(0)\rangle_{NVE}$. Finally, we also constructed the energy gap - coupling cross-correlation function, $\langle \delta\Delta E(t)\delta V(0)\rangle_{NVE}$, using a similar procedure. Plots for one NVE trajectory and the resulting correlation functions are shown in Figure 2.

2. Ansatz *for the coupling*

From our NVE production runs, we extracted the coordinates of the two iron atoms and those of the twelve waters forming the first solvation shell (six in an octahedral configuration around each iron). In principle, one can compute the coupling using an *ab initio* method such as constrained density functional theory with configuration interaction [91–94]; in practice, we found these computations to be quite challenging for this system [95]. As such, we treated the coupling semi-empirically.

Physically, in our test system, electron transfer occurs from the d-orbital manifold of one metal center to the d-orbital manifold of the other metal center; thus, the coupling should physically arise from the interaction between the d-orbitals on the two metals. Additionally, the coupling should decay exponentially with distance [4, 9, 94], and, in order to allow for the existence of conical intersections, should be zero for some nuclear configuration [28]. The overlap of d-orbitals on the two metal centers is an observable with both of these properties that also serves as a direct probe for the interaction between d-orbitals on the metals.

Figure 3 shows four snapshots from a single NVE molecular dynamics trajectory described in the previous section. In each case, we have computed the two d-orbitals that are expected to contribute most significantly to electron transfer between the two atoms using the simple heuristic defined in Appendix C. The figure shows that two things occur over the course of the simulation: (1) the crystal field around each iron ion rotates, causing the d-orbitals on the irons to rotate with respect to each other; and (2) degenerate orbitals mix, causing the orbitals to change shape qualitatively. The latter effect occurs because the distorted octahedral environment causes electron transfer to occur from (and

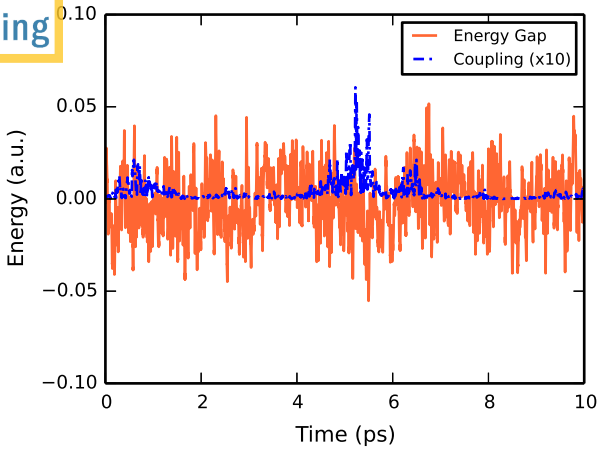

(a)

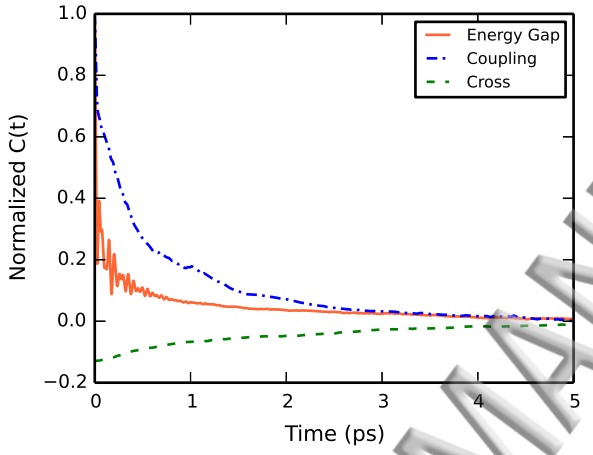

(b)

Figure 2. (a) Energy gaps and couplings fluctuate rapidly on short timescales due to bath motions; the trajectory shown here is one of 300 NVE trajectories sampled from an NVT ensemble used to compute time correlation functions. (b) Energy gap - energy gap and coupling - coupling time autocorrelation functions are computed for this system, as well as energy gap - coupling cross-correlation functions. For illustration only, the correlation functions are normalized (by C(0) for the two autocorrelation functions and by $\sqrt{C_{EG}(0)C_V(0)}$ for the cross-correlation function); unnormalized correlation functions were used in all calculations.

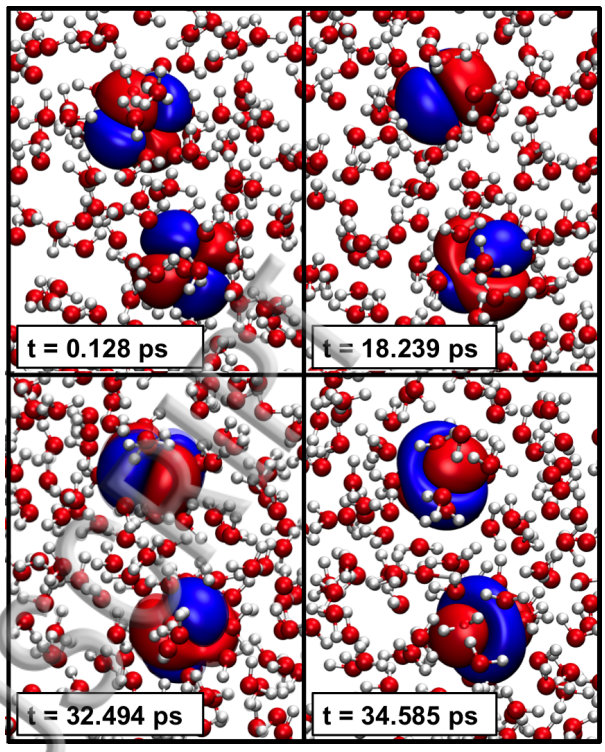

Figure 3. Over the course an NVE trajectory, the orbitals of the two irons change significantly. Due to both rotation of the crystal field around each iron and mixing of degenerate t_{2g} orbitals, both the orientation and qualitative character of the orbitals with respect to one another fluctuate. This causes large fluctuations in the overlap, meaning that even for this simple system, we cannot expect the coupling between the two orbital manifolds to remain constant—it, too, must fluctuate.

to) the lowest energy t_{2g}-like orbital on each iron atom, and the shape of that orbital fluctuates with the environment. The procedure we used to compute overlaps, accounting for both factors, is detailed in Appendix C. We note that the sensitivity of the electronic coupling matrix element to the orientations of the metal atoms has been demonstrated before using more sophisticated wavefunction techniques [61, 96]. Our calculations are intended to capture the same qualitative dynamics at greatly reduced cost.

The overlap of the d-orbitals on the two irons involved in our electron transfer process makes an excellent proxy for a coupling. Like couplings, overlaps decay exponentially with distance, and since the orbitals are rotating with respect to one another throughout the course of the simulation, there is some rotation of the two molecules that will make the orbitals on one iron orthogonal to the orbitals on the other iron, giving an overlap of zero. We thus make an *ansatz* that the coupling is directly proportional to the overlap of the two d-orbitals involved in electron transfer, overlap, S:

$$V = \alpha S \tag{19}$$

We first compute the overlap for the face-to-face configuration described in Ref. [61] at 7.3 Å and fix the undetermined constant α using the reported literature value for the coupling at this distance and this configuration, $V_{lit} = 25.4\,cm^{-1}$

$$\alpha = \frac{V_{lit}}{S_{7.3}} \tag{20}$$

We then apply Equation 19 to compute couplings. It stands to reason that the coupling cannot be constant, even in this simple system: the orbital overlap changes

rapidly with time, causing large fluctuations in the coupling.

3. Computing memory kernels and populations

In order to compute population dynamics and rates, equations 9 and 12 were implemented in FORTRAN 95. Since the spectral density $J(\omega)$ is sampled at a finite number of frequencies from molecular dynamics simulations, we chose to linearly interpolate between the sampled frequencies, as the integrals $Q^{''}(t)$, $R^{'}(t)$, and $S^{''}(t)$ are piecewise analytic for a piecewise linear spectral density. The three remaining integrals ($Q^{'}(t)$, $R^{''}(t)$, and $S^{'}(t)$) are not analytic; we computed these numerically using Simpson's Rule for each piecewise-linear segment, recursively subdividing the intervals until an absolute accuracy of 10^{-15} was reached. In order to avoid numerical divergences, we treated frequencies lower than 10^{-4} a.u. by taking the first 20 terms in the Taylor expansion about $\omega = 0$ of each integrand and evaluating the integral analytically.

Once the kernels were computed, the populations were computed using a standard algorithm for solving Volterra integrodifferential equations of the second kind [97] to solve equation 6 for $P(t) \equiv p_1(t) - p_2(t)$, the difference in population between states 1 and 2 as a function of time.

4. Neglecting the cross-correlation

In Section II C, we hypothesized that the cross-correlation between energy gap and coupling could be neglected in practice. For the hexaaquairon self-exchange simulation discussed in this section, we can justify this approximation as follows. The simulation is symmetric: state $|1\rangle$, where iron(II) is on the left side of the simulation box and iron(III) is on the right side, is indistinguishable from state $|2\rangle$ when each is at equilibrium. Because of this symmetry, $\langle \hat{V} \rangle$ should be identical regardless of whether the sampling is done in state $|1\rangle$ or state $|2\rangle$. However, one can show that

$$\langle \hat{V} \rangle_{1/2} = V_0 \mp \frac{2}{\pi} \int_0^\infty d\omega \frac{J_{cross}(\omega)}{\omega} \tag{21}$$

where V_0 is the Hamiltonian parameter defined in Equation 1, the subscripts on the angle bracket refer to which state the ensemble average is taken in, and the minus sign corresponds to sampling in state $|1\rangle$ / the plus sign in state $|2\rangle$.

It follows that the integral involving $J_{cross}(\omega)$ must be zero. One can show that this directly implies $\langle \delta\Delta E(0)\delta V(0) \rangle = 0$. For the problem studied, we computed this correlation function; in our simulation, $\langle \delta\Delta E(0)\delta V(0) \rangle = -2.9 \times 10^{-7}$, and at all later times it has a magnitude smaller than this, as shown in Figure 2(b). We anticipate that the cross-correlation will have a negligible impact on the dynamics. We will examine the actual effects of the computed cross-correlation function in detail in the resulting section.

5. Computing free energy surfaces

To analyze the position of the conical intersection for our system, we computed diabatic and adiabatic free energy surfaces. For each snapshot in a single NVE trajectory, we formed two lists of coordinates, $\{+\frac{\Delta E}{2}, V\}$ and $\{-\frac{\Delta E}{2}, V\}$, corresponding to the location on the left-hand and righthand potential energy surface of each snapshot along the energy gap and coupling coordinates. We then performed a 2D kernel density estimation using the Scott heuristic along these coordinates to compute $\mathcal{P}_1(\Delta E, V)$ and $\mathcal{P}_2(\Delta E, V)$, the observed probability density functions for the left diabat and the right diabat, respectively. Next, we computed diabatic free energy surfaces as

$$F_i(\Delta E, V) = -k_B T \ln \mathcal{P}_i(\Delta E, V)$$

These are plotted in the subsequent section. We also found it useful to analyze the adiabatic free energy surfaces, which we computed as the eigenvalues of the Hamiltonian

$$\hat{h}(\Delta E, V) = \begin{pmatrix} F_1(\Delta E, V) & V \\ V & F_2(\Delta E, V) \end{pmatrix}$$

We note that along these coordinates, the conical interesection occurs when the energy gap and coupling both vanish simulataneously: At $\{\Delta E = 0, V = 0\}$, the origin of our coordinate system.

IV. RESULTS AND ANALYSIS

A. Spectral densities

The spectral densities computed for iron self-exchange in water are showcased in Figure 4. The energy gap spectral density showcases the strength with which certain bath frequencies drive energy gap fluctuations; similarly, the coupling spectral density showcases the strength with which certain bath frequencies drive coupling fluctuations. The small magnitude of the cross spectral density confirms that the cross-correlation should have a small effect on the dynamics, as expected from theory.

The energy gap spectral density has four features of note: a weak, broad, low-frequency band and three strong, sharp, high-frequency bands. Following the work in Refs. [57] and [59], we interpret these features as bath modes driving outer-sphere and inner-sphere electron transfer, respectively. The three high-frequency

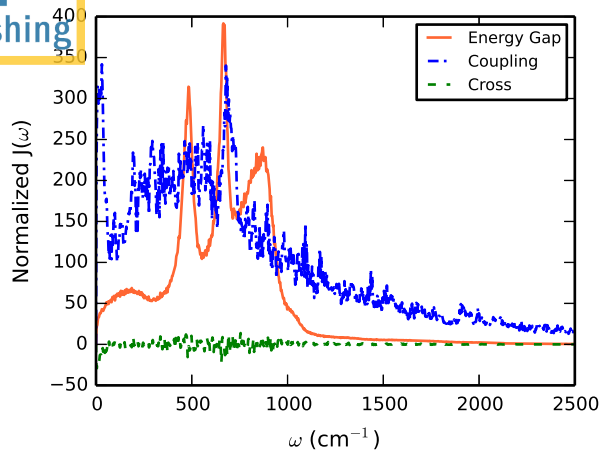

Figure 4. Energy-gap, coupling, and cross spectral densities are computed from the correlation functions shown in Figure 2 via equations 16, 17, and 18, respectively. The energy-gap spectral density has high-frequency structure due to iron-oxygen vibrations—inner-sphere bath modes. While the coupling spectral density shows less structure, there is still substantial off-diagonal system-bath coupling at low and higher frequencies. For illustration purposes, the spectral densities shown are computed from the normalized correlation functions; unnormalized spectral densities were used in dynamics calculations.

bands can be assigned to typical vibrational frequencies observed in hexaaquairon complexes [98], including Fe-O stretching around ∼500 cm^{-1} and H_2O rocking around ∼750 cm^{-1}. The role of outer-sphere bath modes and inner-sphere bath modes in driving iron self-exchange electron transfer has long been a subject of debate [55–61, 99–101], with a consensus that both types of modes can play a role but that coupling-driven outer-sphere electron transfer often plays the bigger role. We observe here both modes of electron transfer driven by energy gap fluctuations occur: slow bath librations drive outer-sphere electron transfer and fast Fe-O and H_2O vibrations drive inner-sphere transfer.

Energy gap fluctuations are not the only force driving electron transfer; though smaller in magnitude, coupling fluctuations also drive electron transfer, shown by the substantial magnitude of the coupling spectral density. Bath modes that drive fluctuations in the coupling tend to be lower-frequency in nature; in the present case, coupling fluctuations are coupled to iron-iron separation distance and the relative orientation of the irons' ligands with respect to one another. In principle, these coupling fluctuations may be correlated to energy gap fluctuations, as, according to our *ansatz* for the coupling, both result from a shifting charge distribution caused by fluctuating solvent motions. However, due to the use of the diabatic representation for our dynamics simulations, changes in the charge density along the reaction coordinates are unlikely: diabatic states do not change appreciably along a reaction coordinate [94].

B. Thermal dynamics

We begin our analysis by examining the dynamics that arise when starting from the thermal initial condition. Using the spectral densities presented above with the memory kernels presented in Equations A26 and A27 in Appendix A, we solved the generalized master equation (Equation 6) to generate electron transfer dynamics for the ground-state electron transfer process. Though we have derived expressions for the non-Condon kernels through fourth-order in perturbation theory, we limit our dynamical treatment for this sample problem to second order, as the average coupling for this system is known to be small [61]. The results are shown in Figure 5. The Condon and non-Condon kernels produce essentially identical short-time dynamics: Both show a very short oscillation for approximately 5 fs before plateauing. The timescale of these oscillations corresponds with the timescale of the fastest bath mode observed in the spectral density, indicating that this fast inner-sphere bath motion drives a small amount of initial electron transfer.

Additionally, once the populations plateau around ∼5 fs, the Condon and non-Condon curves run parallel to one another, indicating that both decay towards equilibrium at the same rate. Non-Condon effects thus conclusively do not affect short-time or long-time electron transfer dynamics for the ground state iron(II)/iron(III) self-exchange reaction—an observation consistent with decades of literature on this reaction [55–64]. We note that whether or not we neglect the cross-correlation, the non-Condon terms have an almost negligible effect on the dynamics.

The unimportance of non-Condon effects for dynamics resulting from the thermal initial condition suggests that the conical intersection is far from the minimum energy path connecting the two wells of the ground-state adiabatic potential energy surface. In order to test this hypothesis, we construct the two diabatic *free* energy surfaces, as well as the ground- and excited-state adiabatic free energy surfaces that result from diagonalizing the 2x2 diabatic Hamiltonian. While ideally potential energy surfaces would be used to study the relative importance of a conical intersection, potential energy surfaces are very high-dimensional. Additionally, the Condon reaction path exists on the free energy surfaces and not the potential energy surfaces. We thus examine free energy surfaces purely for illustrative purposes.

The computed free energy surfaces are shown in Figure 6. We observe from the diabatic surfaces in Figure 6(a) that the major axes of the paraboloid diabats do not align with the chosen reaction coordinates, suggesting that a finite—albeit small—cross-correlation between energy gap and coupling is present in our data. The adiabatic surfaces reveal even more. The conical intersection in this problem, marked on each plot with a bold black 'X', is relatively far from the minimum free energy path connecting the minima of the ground-state adiabat. This confirms our earlier hypothesis: the coni-

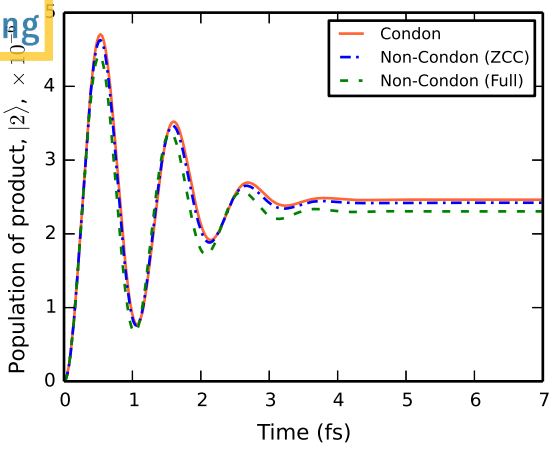

Figure 5. Ground-state iron(II)/Iron(III) electron transfer dynamics using the *thermal* initial condition. Non-Condon (ZCC) dynamics are computed as described in Section II C. The population of the product diabat is plotted as a function of time. The system is initially entirely in electronic state $|1\rangle$, and the bath is initial in thermal equilibrium with this same state ($|1\rangle$). This choice of initial conditions corresponds to the ground-state electron transfer reaction. After a high-frequency bath mode causes a small amount of initial electron transfer, both Condon and non-Condon kernels plateau at a population near 0 and relax towards equilibrium ($p_2 = 0.5$) at the same rate, indicating that non-Condon effects have negligible impact on the ground-state electron transfer process—regardless of whether or not the energy gap - coupling cross-correlation is neglected.

cal intersection is not expected to play a significant role in the thermal electron transfer problem.

The excited-state adiabat, however, tells a different story. The conical intersection here is located extremely close to the minimum of the excited state adiabat, suggesting that including non-Condon effects is essential to adequately describe ultrafast electron transfer dynamics originating on the excited state—a state very similar to that of our nonequilibrium initial condition proposed in Section II D. Thus, based on this result, we now turn our attention to studying how non-Condon effects may influence ultrafast passage through a conical intersection by looking at electron transfer dynamics using the nonequilibrium initial condition.

We wish to stress that the 'nonequilibrium' initial condition is in no way an initial condition that can be experimentally prepared via optical excitation for the iron(II) - iron(III) system under study. In this system, there are many low-lying excited states that would interfere with the preparation of the described state. Additionally, the oscillator strength of the intervalence transition described to reach the nonequilibrium state in our prepared 'nonequilibrium' initial condition is very small, if not zero. For these reasons, the preparation of this initial condition for this system is artificial: nobody has ever observed this kind of transition exper-

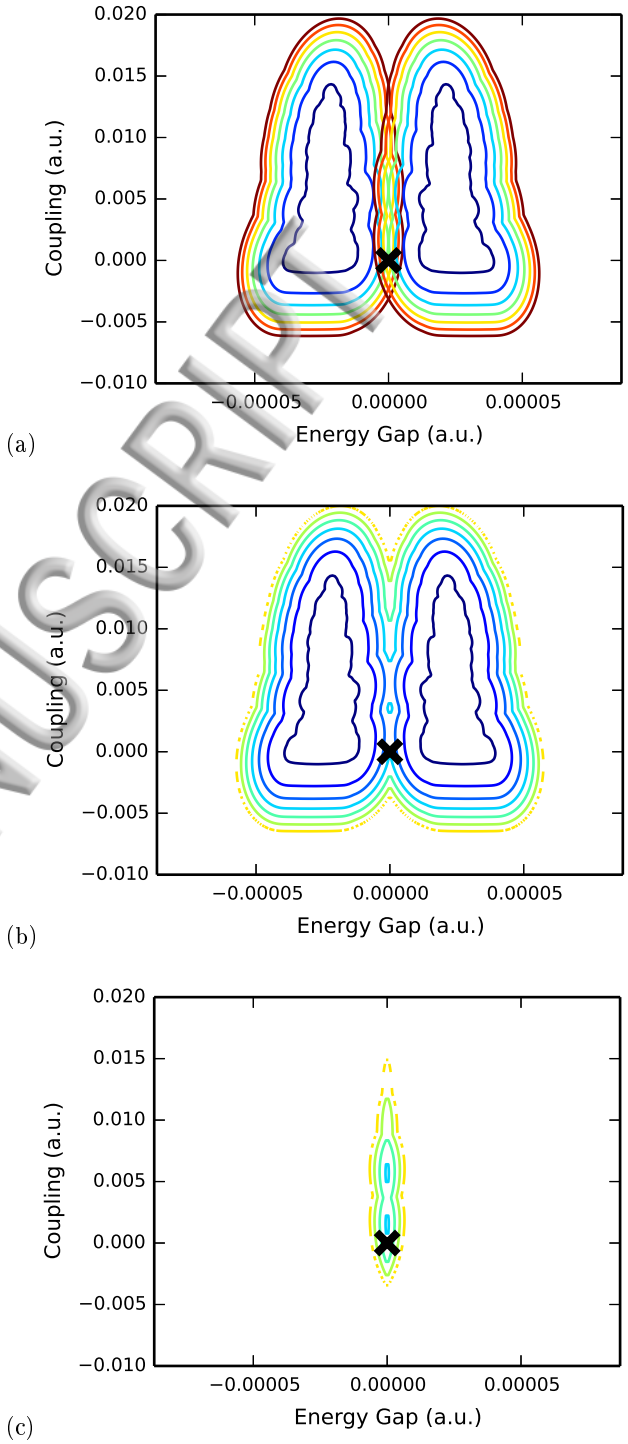

Figure 6. Free energy surfaces along the energy gap and coupling coordinates for iron(II) / iron(III) electron transfer. The location of the conical intersection in each plot is marked with a solid black X. (a) Diabatic free energy surfaces show a small cross-correlation between energy gap and coupling. (b) The lower adiabatic free energy surface. The location of the conical intersection is far from the minimum free energy path between minima, so the conical intersection does not play a role in thermal dynamics. (c) The upper adiabatic free energy surface. The conical intersection is near the minimum of the upper adiabat, so ultrafast passage from the upper adiabat to the lower should be observed for any initial nonequilibrium state originating close to this point.

imentally. Nevertheless, we expect that the dynamics attained with this initial state *could* be representative of optically-induced dynamics in other condensed-phase systems, and thus present these results as a proof-of-principle for the method underlying the dynamics. For the time being, these effects should be thought of strictly as an analogy.

C. Ultrafast nonequilibrium dynamics

Figure 7(a) showcases the short-time dynamics generated by the spectral densities in Figure 4. Plotted here are the populations of the product diabats as a function of time computed using the kernels in Equation 15. The dynamics show several features, including a dip at approximately 15 fs and another dip at approximately 40 fs before a long, slow relaxation to equilibrium. We suspect the first dip is due to a small amount of inner-sphere transfer from the Fe-O stretching mode, and the second dip is due to the onset of slow outer-sphere population transfer. Though the curves appear flat after approximately 60 fs, their slopes are extraordinarily small but non-zero, indicating the transition of the electron transfer from a dynamical process to a rate process.

One can see quite clearly the role of the conical intersection in this problem: non-Condon effects appreciably increase the amount of initial electron transfer from reactant diabat to product diabat. Additionally, non-Condon effects strictly slow down diabatic population transfer (and thus, since this reaction occurs in the Marcus normal regime, speed up adiabatic transfer)—in line with the observation made in Section II D. We note that non-Condon effects do not seem to play a role until after the dip at 40 fs. This result is consistent with our computed spectral densities in Figure 4, which indicate that only slow low-frequency bath modes contribute to fluctuations in the coupling. The fact that the non-Condon effects "turn on" after this time is simply a reflection of the result that for this problem, there are no high-frequency peaks in the coupling spectral density.

Unfortunately, because outer-sphere electron transfer dominates and $\langle V \rangle_{rms}$ is very small for this system, the magnitude of population transfer over the first 100 femtoseconds is small. Nevertheless, examining this system provides an important benchmark: if $\langle V \rangle_{rms}$ were bigger, non-Condon effects would play a vital role in population transfer. This can be seen by scaling $\langle V \rangle_{rms}$ by a factor of 10 so that it has a value of approximately 0.1 eV (a reasonable size for a coupling in, say, an organic charge-transfer system), and scaling the fluctuations in the coupling appropriately. The resulting dynamics are shown in Figure 7(b)—showcasing appreciable diabatic population transfer over the first 100 femtoseconds. In the case where the coupling is larger (though still small enough that we can neglect fourth-order effects), non-Condon effects prevent 0.5% of the population from switching diabats by the time a slow relaxation towards equilibrium is reached at approximately 55 fs—a non-

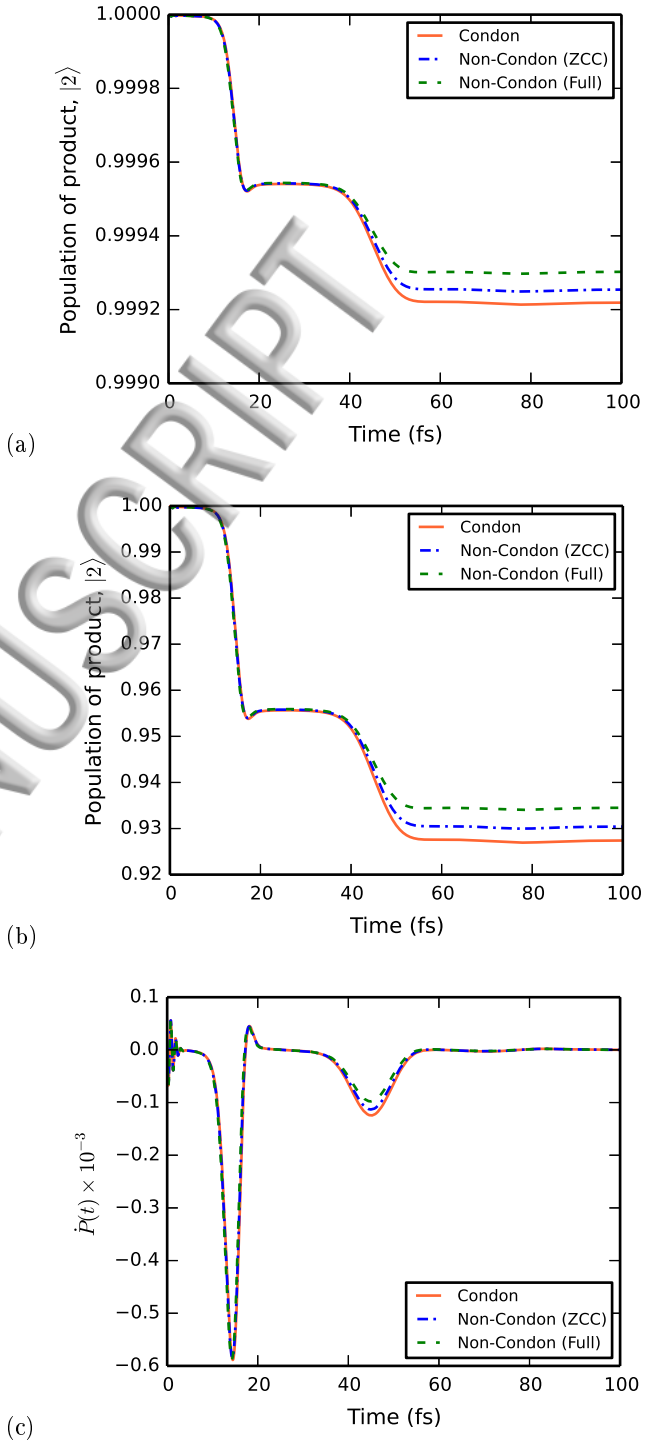

Figure 7. (a) Nonequilibrium Condon and non-Condon dynamics for hexaaquairon(II/III) self-exchange, with $\langle V \rangle_{rms} = 34.5$ cm^{-1}. Non-Condon (ZCC) dynamics are computed as described in Section II C. Non-Condon effects are appreciable, even though charge-transfer is slow due to the small value of $\langle V \rangle_{rms}$ for this system. (b) If the coupling used is instead $\langle V \rangle_{rms} = 345$ cm^{-1}—a reasonable size for many condensed-phase charge-transfer systems—it becomes readily apparent that non-Condon effects are required to recover quantitative population transfer, and that cross-correlation plays only a small role. (c) The instantaneous rate of change of the population difference between the two states as a function of time, $\dot{P}(t)$, for the case depicted in (b).

negligible amount.

Despite the very small magnitude of the cross-correlation function in Figure 2 and the resulting cross spectral density in Figure 4, and despite our argument that the cross-correlation should be rigorously zero for this problem, we observe that the cross-correlation provides a modest effect on population dynamics. We can think of two possible explanations for this inconsistency. The first is that we may be inconsistent in assigning the phase of V, leading to a spurious cross-correlation. This effect may be magnified when we compute $\delta V(t) \equiv V(t) - \langle V \rangle$, as $\langle V \rangle$ is difficult to compute correctly. Because the phase of V is arbitrary, if we were to include all second order effects (including cross-correlation), it shouldn't matter how we choose the sign of V. We believe that the result that includes cross-correlation is likely indicative of the 'true' curve, as it would appear if we assigned the 'right' sign to V at every time point and neglected the cross correlation. In that scenario, the cross-correlation would be zero, but the coupling-coupling autocorrelation function would be summarily different, capturing all of the effects that we see when we include the cross-correlation.

The second possibility is that some of the inner-sphere reorganization is correlated to the coupling: some mode that changes the energy gap also changes the shape of the orbital involved, leading to correlation between V and ΔE. Regardless of which is responsible for the observed cross-correlation phenomenon, we note that the observed correlation (i.e., the cross-correlation spectral density) is small, so it seems reasonable to neglect these terms, as least in higher-order (i.e. fourth-order and beyond) contributions to the dynamics.

We conclude our discussion by observing that for the system studied, non-Condon effects do not appear to change the *overall* long-time rate of electron transfer (despite affecting the *instantaneous* rate significantly at short times). Figure 7(c) contains a plot of the rate of change of the diabatic populations with time for both the Condon case and the non-Condon case. While the two curves do not align at short and intermediate times, they are identical at long times—consistent with the Nonequilibrium Fermi's Golden Rule result detailed in Refs. [79] and [68]. We do not know if this is a general phenomenon or one that is system-specific; nevertheless, the observation that for at least some systems non-Condon effects appear to have negligible impact on rates is important and should be noted.

V. CONCLUSIONS

In this paper, we have asserted that even in simple electron transfer systems, the Condon approximation will often result in short-time dynamics that are not quantitatively accurate. We have shown that for hexaaquairon self-exchange in water, the coupling is expected to fluctuate significantly on short (∼10-100 fs) timescales. In more complex systems, this fluctuation in the coupling is necessary in order to predict ultrafast nonequilibrium dynamics accurately, including such phenomena as conical intersections. By developing a formalism based on the linear vibronic coupling Hamiltonian, we show that in iron self-exchange, for reasonable values of $\langle V \rangle_{rms}$, non-Condon effects are expected to substantially alter the amount of initial nonequilibrium charge transfer that occurs before the system begins its slow relaxation towards equilibrium.

We hope to extend our work to provide more accurate dynamics by going to higher-orders in perturbation theory, so that we can safely tackle the intermediate- and strong-coupling regimes with conviction. We also wish to examine the effect of using polarizable force fields on the resulting spectral densities, as polarizable force fields are necessary for quantitatively-accurate solvent reorganization and thus photochemical dynamics [102].

Ultimately, we hope to use our formalism to study chemical systems with conical intersections. Many chemical systems contain conical intersections that can be directly modeled [103–107]. Direct observation of molecular relaxation through conical intersections via a mapping on to the linear vibronic coupling Hamiltonian could potentially allow us to make predictions about nonradiative decay rates in photochemistry—an essential component to first-principles prediction of quantum yields. Even an approximate description of such photochemical dynamics will be invaluable towards predicting the photochemical properties of small molecules in the condensed phase.

ACKNOWLEDGMENTS

M. G. M. would like to thank Valerie Vaissier and Prof. Koji Ando for very helpful discussions and data; additionally he would like to thank the NSF GRFP program for funding. This work was supported by NSF grant CHE-1464804.

Appendix A: Derivation of the Nonequilibrium Kernels to Fourth-order $K^{(2)}$ and $K^{(4)}$

We present here an explicit derivation of the nonequilibrium memory kernels for the linear vibronic coupling Hamiltonian to fourth-order in perturbation theory. The lack of explicit time dependence in $\hat{H}_{LVC}$ implies that the overall density matrix of the system $\rho(t)$ evolves as

$$\rho(t) = e^{-it\hat{H}_{LVC}}\rho(0)e^{it\hat{H}_{LVC}} \tag{A1}$$

Since we are only interested in the populations in states $|1\rangle$ and $|2\rangle$, we can trace out the bath modes and write:

$$p_1(t) = \mathrm{Tr}_{bath}\left[\rho(t)|1\rangle\langle 1|\right] \tag{A2}$$

$$p_2(t) = \mathrm{Tr}_{bath}\left[\rho(t)|2\rangle\langle 2|\right] = 1 - p_1(t) \tag{A3}$$

Treating the off-diagonal elements of $\hat{H}_{LVC}$ as perturbations allows us to expand $p_1(t)$ as a power series in terms of the off-diagonal elements. If we start purely at state $|1\rangle$, we have:

$$\rho(0) = \begin{pmatrix} \rho_B & 0 \\ 0 & 0 \end{pmatrix} \tag{A4}$$

where ρ_B is the initial bath density matrix. We discuss two initial conditions:

1. The nonequilibrium initial condition, $\rho_B = \frac{e^{-\beta \hat{h}_2}}{\mathrm{Tr}\left[e^{-\beta \hat{h}_2}\right]}$, where the system has been electronically excited from $|2\rangle$ to $|1\rangle$, but the bath modes have not yet had an opportunity to relax from their initial thermal equilibrium with $|2\rangle$.

2. The thermal initial condition, $\rho_B = \frac{e^{-\beta \hat{h}_1}}{\mathrm{Tr}\left[e^{-\beta \hat{h}_1}\right]}$, where the system starts in State 1 ($p_1(0) = 1$) in equilibrium with the bath.

We focus most of our discussion on the nonequilibrium initial condition. This initial condition implies $p_1(0) = 1$ and so we have

$$p_1(t) = 1 + p_1^{(2)}(t) + p_1^{(4)}(t) \dots \tag{A5}$$

where $p_1^{(2n)}(t)$ is the $2n^{\text{th}}$ order term in the series (odd order terms are zero with these initial conditions), which are all zero at $t = 0$ and can be determined using time-dependent perturbation theory.

We then define $\hat{h}_1, \hat{h}_2, \hat{O}(t)$ and $F_{2n}(t_1, t_2)$ such that

$$\hat{H}_{LVC} = \begin{pmatrix} \hat{h}_1 & V_0 + \sum_j V_j \hat{x}_j \\ V_0 + \sum_j V_j \hat{x}_j & \hat{h}_2 \end{pmatrix} \tag{A6}$$

$$\hat{O}(t) \equiv e^{i\hat{h}_1 t} \left(V_0 + \sum_j V_j \hat{x}_j \right) e^{-i\hat{h}_2 t} \tag{A7}$$

$$F_{2n}(t_1, t_2 \dots t_{2n}) \equiv \mathrm{Tr}\left[\prod_{i=1}^{n} \left(O(t_{2i-1}) O^\dagger(t_{2i}) \right) \rho_B(0) \right] \tag{A8}$$

The populations $p^{(2n)}(t)$ can be obtained by integrating traces $F_{2n}(t_1, t_2 \dots t_{2n})$, which can be evaluated using a Gaussian coherent state basis as described in our previous work [54]. Consequently, we find that for nonequilibrium ρ_B we have:

$$\begin{aligned} F_2(t_1, t_2) = &\left((V_0 + \alpha(t_1, t_2)) (V_0 + \beta(t_1, t_2)) \right. \\ &\left. + \gamma(t_1 - t_2) \right) f_2(t_1, t_2) \end{aligned} \tag{A9}$$

where

$$f_2(t_1, t_2) = \exp\left[-i\epsilon(t_1 - t_2) - Q'(t_1 - t_2) - i\phi(t_1, t_2) \right] \tag{A10}$$

and we define

$$\phi(t_1, t_2) \equiv Q''(t_1 - t_2) - 2Q''(t_1) + 2Q''(t_2) \tag{A11}$$

$$\alpha(t_1, t_2) \equiv 2R'(t_1) - R'(t_1 - t_2) + iR''(t_1 - t_2) \tag{A12}$$

$$\beta(t_1, t_2) \equiv 2R'(t_2) - R'(t_1 - t_2) + iR''(t_1 - t_2) \tag{A13}$$

$$\gamma(t) \equiv S'(t) - iS''(t) \tag{A14}$$

Here, $Q'(t)$, $Q''(t)$, $R'(t)$, $R''(t)$, $S'(t)$, and $S''(t)$ have been defined previously, in Equations 11 – 14. Note that for the spin-boson Hamiltonian, when the coupling is a constant (V_0), $\alpha = \beta = \gamma = 0$. In the case where we can neglect the cross-correlation, $R'(t) = R''(t) = 0$ and the above equations simplify:

$$F_2(t_1, t_2) \approx T_2(t_1, t_2) f_2(t_1, t_2) \tag{A15}$$

where $f_2(t_1, t_2)$ is defined in Equation A10 and we define

$$\begin{aligned} T_2(t_1, t_2) &\equiv \left(V_0^2 + \gamma(t_1 - t_2) \right) \\ &= \left(\langle V^2 \rangle + \gamma(t_1 - t_2) - \gamma(0) \right) \end{aligned} \tag{A16}$$

When we can neglect cross-correlation, we can analogously write the fourth-order bath correlation function F_4 as

$$F_4(t_1, t_2, t_3, t_4) = T_4(t_1, t_2, t_3, t_4) f_4(t_1, t_2, t_3, t_4) \tag{A17}$$

where

$$f_4(t_1, t_2, t_3, t_4) = \frac{f_2(t_1, t_2) f_2(t_2, t_3) f_2(t_3, t_4) f_2(t_1, t_4)}{f_2(t_1, t_3) f_2(t_2, t_4)} \tag{A18}$$

and

$$\begin{aligned} T_4(t_1, t_2, t_3, t_4) = &T_2(t_1, t_2) T_2(t_3, t_4) + T_2(t_1, t_3) T_2(t_2, t_4) \\ &+ T_2(t_1, t_4) T_2(t_2, t_3) - 2V_0^4 \end{aligned} \tag{A19}$$

All that remains is to connect the bath correlation functions F_2 and F_4 to the memory kernels $K^{(2)}$ and $K^{(4)}$. From perturbation theory, these bath correlation functions are related to the populations by

$$p_1^{(2)}(t) = -2\int_0^t dt_1 \int_0^{t_1} dt_2 \mathrm{Re}\left[F_2(t_1,t_2)\right] \tag{A20}$$

$$p_1^{(4)}(t) = 2\int_0^t dt_1 \int_0^{t_1} dt_2 \int_0^{t_2} dt_3 \int_0^{t_3} dt_4 \mathrm{Re}\left[F_2(t_1,t_2,t_3,t_4)\right] + \int_0^t dt_1 \int_0^{t_1} dt_2 \int_0^{t} dt_3 \int_0^{t_3} dt_4 F_2(t_2,t_1,t_3,t_4) \tag{A21}$$

The memory kernels $K^{(2n)}(t,t_1)$ cannot be uniquely determined; however, kernels consistent with Equations A20 and A21 can be obtained by expanding the rate equations (Equation 6) in the coupling $\hat{V}$ and matching orders in perturbation theory by analogy. This results in the kernels

$$K_1^{(2)}(t,t_1) = 2\mathrm{Re}\left[F_2(t,t_1)\right] \tag{A22}$$

which is consistent with A20, and

$$K_1^{(4)}(t,t_1) = -2\mathrm{Re}\left[\int_0^{t_1} dt_2 \int_0^{t_2} F_4(t,t_1,t_2,t_3)dt_3 + \int_0^{t} dt_2 \int_0^{t_2} F_4(t_1,t,t_2,t_3)dt_3\right] + K_+^{(2)}(t,t_1)\int_0^{t_1} dt_2 \int_0^{t_2} K_1^{(2)}(t_2,t_3)dt_3 \tag{A23}$$

which is consistent with A21. This analysis also holds for the backward kernel K_2 under the substitution $\epsilon \to -\epsilon$.

We briefly consider the thermal initial conditions discussed at the start of this section. Under this set of initial conditions, only the form of f_2 changes on moving from nonequilibrium initial conditions to thermal conditions; thus, all of the equations described in this section can be used to compute memory kernels under thermal initial conditions, making the substitution:

$$f_2(t_1,t_2) \to f_2^{th}(t_1 - t_2) \tag{A24}$$

$$f_2^{th}(t) = \exp\left[-i\epsilon t - Q'(t) - iQ''(t)\right] \tag{A25}$$

Importantly, the non-Condon piece of the kernels, T_2, remains the same so long as cross-correlations between energy gap fluctuations and coupling fluctuations can be neglected. The fourth-order kernels can be derived making the same substitution for f_2 and using equations A18 and A19.

For reference, the full second-order thermal kernel is

$$K_{th}^{(2)}(t) = K_{th,c}^{(2)}(t) + K_{th,nc}^{(2)}(t)$$

where $K_{th,c}^{(2)}(t)$ is the Condon piece,

$$K_{th,c}^{(2)}(t) = 2V_0^2 \exp\left[-Q'(t)\right]\cos\left[Q''(t) \pm \epsilon t\right] \tag{A26}$$

and $K_{th,nc}^{(2)}(t)$ is the non-Condon piece,

$$\begin{aligned} K_{th,nc}^{(2)}(t) = 2\exp\left[-Q'(t)\right]\Big[&S'(t)\cos(Q''(t)\pm\epsilon t) - S''(t)\sin(Q''(t)\pm\epsilon t) \\ &+ \left(\left(R'(t)\right)^2 - \left(R''(t)\right)^2\right)\cos(Q''(t)\pm\epsilon t) - 2R''(t)R'(t)\sin(Q''(t)\pm\epsilon t) \\ &\mp 2V_0\left(R'(t)\cos\left(Q''(t)\pm\epsilon t\right) - R''(t)\sin\left(Q''(t)\pm\epsilon t\right)\right)\Big] \end{aligned} \tag{A27}$$

where the top sign is for the forward kernel, K_1, and the bottom sign is for the reverse kernel, K_2.

Appendix B: Time-domain Padé resummation

Previously, we have explored several different resummation schemes [54] in Fourier space for second and fourth-order dynamical memory kernels. We concluded that while Padé resummation gives the most accurate resummed kernel in certain regions of parameter space; in other regions, in fails entirely, giving divergent dynamics at long times. A detailed analysis of Padé resummations for this problem [77] has made explicit certain conditions on the second-order and fourth-order kernels that predict whether or not Padé resummation will blow up or not; using these conditions, Reichman et al have shown that Padé resummation is expected to behave

This manuscript was accepted by J. Chem. Phys. Click here to see the version of record.

poorly at low temperatures and high system-bath coupling.

Both our and their primary arguments about why the Padé resummation fails are that the Padé resummation is a rational resummation, and certain sets of bath parameters cause singularities in the resummed kernel in Fourier (or Laplace) space, leading to long-time divergences. A Padé resummed kernel can be written in Laplace space as

$$K_{Padé}(s) = \frac{\left[K^{(2)}(s)\right]^2}{K^{(2)}(s) - K^{(4)}(s)} \tag{B1}$$

Besides the methods that have been investigated previously, there is one additional method that can be used to potentially smooth the divergences inherent to a rational approximation: Get rid of the denominator. We do so by first rearranging equation B1:

$$K_{Padé}(s) = K^{(2)}(s) + \phi(s)K_{Padé}(s) \tag{B2}$$

where we have defined

$$\phi(s) \equiv \frac{K^{(4)}(s)}{K^{(2)}(s)} \tag{B3}$$

We then analytically inverse Laplace transform equations B2 and B3, recognizing that a multiplication in the Laplace domain is a convolution in the time domain:

$$K^{(4)}(t) = \int_0^t dt^{'} \phi(t - t^{'})K^{(2)}(t^{'}) \tag{B4}$$

$$K_{TDP}(t) = K^{(2)}(t) + \int_0^t dt^{'} \phi(t - t^{'})K_{Padé}(t^{'}) \tag{B5}$$

where the acronym TDP stands for "time-domain Padé." We can thus carry out Padé resummation in the time domain by solving equation B4 numerically for $\phi(t)$, and then using that solution to solve equation B5 numerically for $K_{TDP}(t)$.

Appendix C: Computing the overlap between d-orbitals

According to crystal field theory, the electron transfer in this problem is from the t_{2g} manifold of one iron to the t_{2g} manifold of another iron; thus, the d-orbitals overlaps relevant to our problem are the overlaps of d_{xy}, d_{xz}, and d_{yz} on one iron atom with those of d_{xy}, d_{xz}, and d_{yz} on the other iron atom. Since there are manifolds of orbitals and thus 9 relevant overlaps involves in this electron transfer process, we choose to use as S in equation 19 the magnitude of the largest eigenvalue of the 3x3 overlap matrix in the subspace of the t_{2g} manifolds.

Evaluation of these overlaps not simple: it is confounded by the rotation of one iron with respect to the other. The process by which we arrive at the eigenvalue of the $t_{2g} - t_{2g}$ subspace of the overlap matrix can be enumerated as follows:

1. Using a STO-16g basis set which we parameterized to fit a Slater orbital with an exponent of 6.25 (as determined by Slater's Rules [108]), compute the 36 overlaps of the *unrotated* Cartesian d-orbitals d_{xx},d_{xy},d_{yy},d_{xz},d_{yz}, and d_{zz} on one iron atom with the other, and build the untransformed cartesian overlap matrix $S_{ij} = \langle d_i^{Fe(II)} | d_j^{Fe(III)} \rangle$.

2. Build the two rotation matrices $\mathbf{R_1^{'}}$ and $\mathbf{R_2^{''}}$ that transform the Cartesian basis vectors into the principle axes of molecule 1 and the principle axes of molecule 2, respectively. The principle axes can be determined from diagonalization of the inertia tensors for each hexaaquairon molecule. Special care must be taken to reorder the principle axes at each simulation step to ensure, e.g., that the rotated x axis remains in the x position and do not flip to the y or z position.

3. Build the matrices $\mathbf{T_{d1}^{'}}$ and $\mathbf{T_{d2}^{''}}$ that transform the Cartesian d-orbitals in the lab frame to the rotated frame for each molecule. These are 6x6 matrices for quadratic and bilinear coordinates which can be constructed using appropriate combinations of elements from the linear rotation matrices $\mathbf{R_1^{'}}$ and $\mathbf{R_2^{''}}$.

4. Build the matrix $\mathbf{Y}$ that transforms the Cartesian d-orbitals into the spherical d-orbitals

5. The rotated overlaps in the spherical harmonic basis can then be computed as

$$\mathbf{S}_{rot} = \mathbf{Y}^T \left[\mathbf{T_{d1}^{'}}\right]^T \mathbf{S}\mathbf{T_{d2}^{''}}\mathbf{Y} \tag{C1}$$

Once the 6x6 $\mathbf{S}_{rot}$ is computed, the 3x3 block corresponding to the t_{2g} subspace, $\mathbf{S}_{rot}^{t2g}$, can be excised. The numerical value S to be used in equation 19 can be computed as

$$S = \max\left(\text{abs}\left(\text{eig}\left(\mathbf{S}_{rot}^{t2g}\right)\right)\right) \tag{C2}$$

[1] R. A. Marcus, J. Chem. Phys. **24**, 966 (1956).

[2] R. A. Marcus, J. Chem. Phys. **43**, 679 (1965).

[3] R. A. Marcus, Angew. Chem. Int. Ed. (English) **32**, 1111 (1993).
[4] M. D. Newton and N. Sutin, Annu. Rev. Phys. Chem. **35**, 437 (1984).
[5] G. L. Closs, L. T. Calcaterra, N. J. Green, K. W. Penfield, and J. R. Miller, J. Phys. Chem. **90**, 3673 (1986).
[6] G. J. Kavarnos and N. J. Turro, Chem. Rev. **86**, 401 (1986).
[7] D. Y. Yang and R. I. Cukier, J. Chem. Phys. **91**, 281 (1989).
[8] E. Akesson, G. C. Walker, and P. F. Barbara, J. Chem. Phys. **95**, 4188 (1991).
[9] P. F. Barbara, T. J. Meyer, and M. A. Ratner, J. Phys. Chem. **100**, 13148 (1996).
[10] G. Ramakrishna and H. N. Ghosh, J. Phys. Chem. B **105**, 7000 (2001).
[11] J. S. Kretchmer and T. F. Miller, Inorg. Chem. **55**, 1022 (2016).
[12] P. Song, Y. Li, F. Ma, T. Pullerits, and M. Sun, Chem. Rec. **00**, 1 (2016).
[13] A. O. Caldeira and A. J. Leggett, Ann. Phys. **149**, 374 (1983).
[14] D. E. Makarov and N. Makri, Phys. Rev. A **48**, 3626 (1993).
[15] D. E. Makarov and N. Makri, Chem. Phys. Lett. **221**, 482 (1994).
[16] M. Topaler and N. Makri, J. Chem. Phys. **101**, 7500 (1994).
[17] N. Makri, J. Math. Phys. **36**, 2430 (1995).
[18] N. Makri and D. E. Makarov, J. Chem. Phys. **102**, 4600 (1995).
[19] N. Makri and D. E. Makarov, J. Chem. Phys. **102**, 4611 (1995).
[20] M. Thoss, H. Wang, and W. H. Miller, J. Chem. Phys. **115**, 2991 (2001).
[21] H. Wang, M. Thoss, and W. H. Miller, J. Chem. Phys. **115**, 2979 (2001).
[22] A. Ishizaki and Y. Tanimura, J. Phys. Soc. Jpn. **74**, 3131 (2005).
[23] Y. Tanimura, J. Phys. Soc. Jpn. **75**, 082001 (2006).
[24] A. Leggett, S. Chakravarty, A. Dorsey, M. Fisher, A. Garg, and W. Zwerger, Rev. Mod. Phys. **59**, 1 (1987).
[25] D. R. Reichman, F. L. H. Brown, and P. Neu, Phys. Rev. E **55**, 2328 (1997).
[26] X. Song, H. Wang, and T. Van Voorhis, J. Chem. Phys. **129**, 144502 (2008).
[27] A. Nitzan, *Chemical Dynamics in Condensed Phases: Relaxation, Transfer, and Reactions in Condensed Molecular Systems* (Oxford Univ. Press, Oxford, 2006).
[28] J. von Neumann and E. P. Wigner, Phys. Z. **30**, 467 (1929).
[29] W. Domcke, D. R. Yarkony, and H. Koppel, eds., *Conical Intersections: Theory, Computation and Experiment* (World Scientific Publishing Co. Pte. Ltd., Singapore, 2011).
[30] G. A. Worth and L. S. Cederbaum, Annu. Rev. Phys. Chem. **55**, 127 (2004).
[31] B. G. Levine and T. J. Martínez, Annu. Rev. Phys. Chem. **58**, 613 (2007).
[32] B. G. Levine, J. D. Coe, and T. J. Martínez, J. Phys. Chem. B **112**, 405 (2008).
[33] B. Kaduk and T. Van Voorhis, J. Chem. Phys. **133**, 1 (2010).
[34] S. Matsika and P. Krause, Annu. Rev. Phys. Chem. **62**, 621 (2011).
[35] W. Domcke and D. R. Yarkony, Annu. Rev. Phys. Chem. **63**, 325 (2012).
[36] C. Canuel, M. Mons, F. Piuzzi, B. Tardivel, I. Dimicoli, and M. Elhanine, J. Chem. Phys. **122**, 074316 (2005).
[37] M. S. de Vries and P. Hobza, Annu. Rev. Phys. Chem. **58**, 585 (2007).
[38] J. S. Lim and S. K. Kim, Nat. Chem. **2**, 627 (2010).
[39] M. Chachisvilis and A. H. Zewail, J. Phys. Chem. A **26**, 7408 (1999).
[40] S. Gozem, E. Mirzakulova, I. Schapiro, F. Melaccio, K. D. Glusac, and M. Olivucci, Angew. Chem. Int. Ed. (English) **53**, 9870 (2014).
[41] S. Matsika, J. Phys. Chem. A **108**, 7584 (2004).
[42] S. L. Logunov, V. V. Volkov, M. Braun, and M. A. El-Sayed, Proc. Natl. Acad. Sci. USA **98**, 8475 (2001).
[43] D. Polli, P. Altoè, O. Weingart, K. M. Spillane, C. Manzoni, D. Brida, G. Tomasello, G. Orlandi, P. Kukura, R. A. Mathies, M. Garavelli, and G. Cerullo, Nature **467**, 440 (2010).
[44] G. Zgrablić, A. M. Novello, and F. Parmigiani, J. Am. Chem. Soc. **134**, 955 (2012).
[45] A. Toniolo, G. Granucci, and T. J. Martínez, J. Phys. Chem. A **107**, 3822 (2003).
[46] A. Toniolo, S. Olsen, L. Manohar, and T. J. Martínez, Faraday Discuss. **127**, 149 (2004).
[47] I. Burghardt, L. S. Cederbaum, and J. T. Hynes, Faraday Discuss. **127**, 395 (2004).
[48] R. Spezia, I. Burghardt, and J. T. Hynes, Mol. Phys. **104**, 903 (2006).
[49] I. Burghardt, J. T. Hynes, E. Gindensperger, and L. S. Cederbaum, Physica Scripta **73**, C42 (2006).
[50] I. Burghardt and J. T. Hynes, J. Phys. Chem. A **110**, 11411 (2006).
[51] F. Bernardi, M. Olivucci, and M. A. Robb, Chem. Soc. Rev. **25**, 321 (1996).
[52] J.-L. Brédas, J. E. Norton, J. Cornil, and V. Coropceanu, Accounts Chem. Res. **42**, 1691 (2009).
[53] M. Sparpaglione and S. Mukamel, J. Chem. Phys. **88**, 3263 (1988).
[54] M. G. Mavros and T. Van Voorhis, J. Chem. Phys. **141**, 054112 (2014).
[55] R. A. Kuharski, J. S. Bader, D. Chandler, M. Sprik, M. L. Klein, and R. W. Impey, J. Chem. Phys. **89**, 3248 (1988).
[56] J. S. Bader and D. Chandler, Chem. Phys. Lett. **157**, 501 (1989).
[57] J. S. Bader, R. A. Kuharski, and D. Chandler, J. Chem. Phys. **93**, 230 (1990).
[58] D. Chandler, in *Classical and Quantum Dynamics in Condensed Phase Simulations*, edited by B. J. Berne, G. Ciccotti, and D. F. Coker (World Scientific, Singapore, 1998) Chap. 2, pp. 25–49.
[59] K. Ando, J. Chem. Phys. **106**, 116 (1997).
[60] K. Ando, J. Chem. Phys. **114**, 9470 (2001).
[61] K. M. Rosso, D. M. A. Smith, and M. Dupuis, J. Phys. Chem. A **108**, 5242 (2004).
[62] A. Migliore and M. L. Klein, J. Chem. Theory Comput. **5**, 307 (2009).
[63] C. Drechsel-Grau and M. Sprik, J. Chem. Phys. **136**, 034506 (2012).
[64] P. Zarzycki, S. Kerisit, and K. Rosso, J. Colloid Interf.

Sci. **361**, 293 (2011).
[65] R. L. Fulton and M. Gouterman, J. Chem. Phys. **35**, 1059 (1961).
[66] R. D. Coalson and D. G. Evans, Chem. Phys. **296**, 117 (2004).
[67] S. Jang and M. D. Newton, J. Chem. Phys. **122** (2005), 10.1063/1.1828431.
[68] A. F. Izmaylov, D. Mendive-Tapia, M. J. Bearpark, M. A. Robb, J. C. Tully, and M. J. Frisch, J. Chem. Phys. **135** (2011), 10.1063/1.3667203.
[69] R. Borrelli and A. Peluso, J. Chem. Theory Comput. **11**, 415 (2015).
[70] K.-W. Sun, Y. Fujihashi, A. Ishizaki, and Y. Zhao, J. Chem. Phys. **144**, 204106 (2016).
[71] R. Zwanzig, J. Chem. Phys. **33**, 1338 (1960).
[72] R. Zwanzig, Phys. Rev. **124**, 983 (1961).
[73] R. Zwanzig, Physica **30**, 1109 (1964).
[74] W. C. Pfalzgraff, A. Kelly, and T. E. Markland, J. Phys. Chem. Lett. **6**, 4743 (2015).
[75] M. Cho and R. J. Silbey, J. Chem. Phys. **106**, 2654 (1997).
[76] Z. Gong, Z. Tang, S. Mukamel, J. Cao, and J. Wu, J. Chem. Phys. **142**, 084103 (2015), arXiv:1502.02792.
[77] H.-T. Chen, T. C. Berkelbach, and D. R. Reichman, J. Chem. Phys. **144**, 154106 (2016), arXiv:1603.03712.
[78] S. Chakravarty and A. Leggett, Phys. Rev. Lett. **52**, 5 (1984).
[79] R. D. Coalson, D. G. Evans, and A. Nitzan, J. Chem. Phys. **101**, 436 (1994).
[80] W. R. Cook, D. G. Evans, and R. D. Coalson, Chem. Phys. Lett. **420**, 362 (2006).
[81] Y. Dahnovsky, Phys. Rev. B **73**, 1 (2006).
[82] X. Sun and E. Geva, J. Chem. Phys. **144**, 244105 (2016).
[83] W. R. Cook, R. D. Coalson, and D. G. Evans, J. Phys. Chem. B **113**, 11437 (2009).
[84] Y. Zhao, Y. Yao, and V. Chernyak, J. Chem. Phys. **140**, 161105 (2014).
[85] S. Valleau, A. Eisfeld, and A. Aspuru-Guzik, J. Chem. Phys. **137**, 224103 (2012).
[86] E. Rivera, D. Montemayor, M. Masia, and D. F. Coker, J. Phys. Chem. B **117**, 5510 (2013).
[87] B. Hess, C. Kutzner, D. Van Der Spoel, and E. Lindahl, J. Chem. Theory Comput. **4**, 435 (2008).
[88] W. L. Jorgensen, J. Chandrasekhar, J. D. Madura, R. W. Impey, and M. L. Klein, J. Chem. Phys. **79**, 926 (1983).
[89] T. Darden, D. York, and L. Pedersen, J. Chem. Phys **98**, 10089 (1993).
[90] I. G. Tironi, R. Sperb, P. E. Smith, and W. F. Van Gunsteren, J. Chem. Phys. **102**, 5451 (1995).
[91] Q. Wu and T. Van Voorhis, J. Phys. Chem. A **110**, 9212 (2006).
[92] Q. Wu and T. Van Voorhis, J. Chem. Phys. **125**, 164105 (2006).
[93] Q. Wu, C.-L. Cheng, and T. Van Voorhis, J. Chem. Phys. **127**, 164119 (2007).
[94] T. Van Voorhis, T. Kowalczyk, B. Kaduk, L.-P. Wang, C.-L. Cheng, and Q. Wu, Annu. Rev. Phys. Chem. **61**, 149 (2010).
[95] M. G. Mavros and T. Van Voorhis, J. Chem. Phys. **143** (2015), 10.1063/1.4938103.
[96] D. M. A. Smith, K. M. Rosso, M. Dupuis, M. Valiev, and T. P. Straatsma, J. Phys. Chem. B **110**, 15582 (2006).
[97] T. A. Burton, *Volterra Integral and Differential Equations*, 2nd ed. (Elsevier, 2005).
[98] A. Jarzecki, A. Anbar, and T. Spiro, J. Phys. Chem. A **108**, 2726 (2004).
[99] S. A. Welch, B. L. Beard, C. M. Johnson, and P. S. Braterman, Geochim. Cosmochim. Ac. **67**, 4231 (2003).
[100] P. Sit, M. Cococcioni, and N. Marzari, Phys. Rev. Lett. **97**, 028303 (2006), arXiv:0606310v1 [arXiv:cond-mat].
[101] R. P. Matthews and K. J. Naidoo, J. Phys. Chem. B **114**, 7286 (2010).
[102] A. Warshel, M. Kato, and A. V. Pisliakov, J. Chem. Theory Comput. **3**, 2034 (2007).
[103] M. A. Robb, F. Bernardi, and M. Olivucci, Pure Appl. Chem. **67**, 783 (1995).
[104] D. A. Horke, Q. Li, L. Blancafort, and J. R. R. Verlet, Nat. Chem. **5**, 711 (2013).
[105] S. Lobsiger, M. A. Trachsel, H. M. Frey, and S. Leutwyler, J. Phys. Chem. B **117**, 6106 (2013).
[106] A. Nakayama, S. Yamazaki, and T. Taketsugu, J. Phys. Chem. A **118**, 9429 (2014).
[107] A. J. Musser, M. Liebel, C. Schnedermann, T. Wende, T. B. Kehoe, A. Rao, and P. Kukura, Nat. Phys. **11**, 352 (2015).
[108] A. Szabo and N. Ostlund, *Modern Quantum Chemistry* (Dover Publications, Mineola, 1996) pp. 272–285.

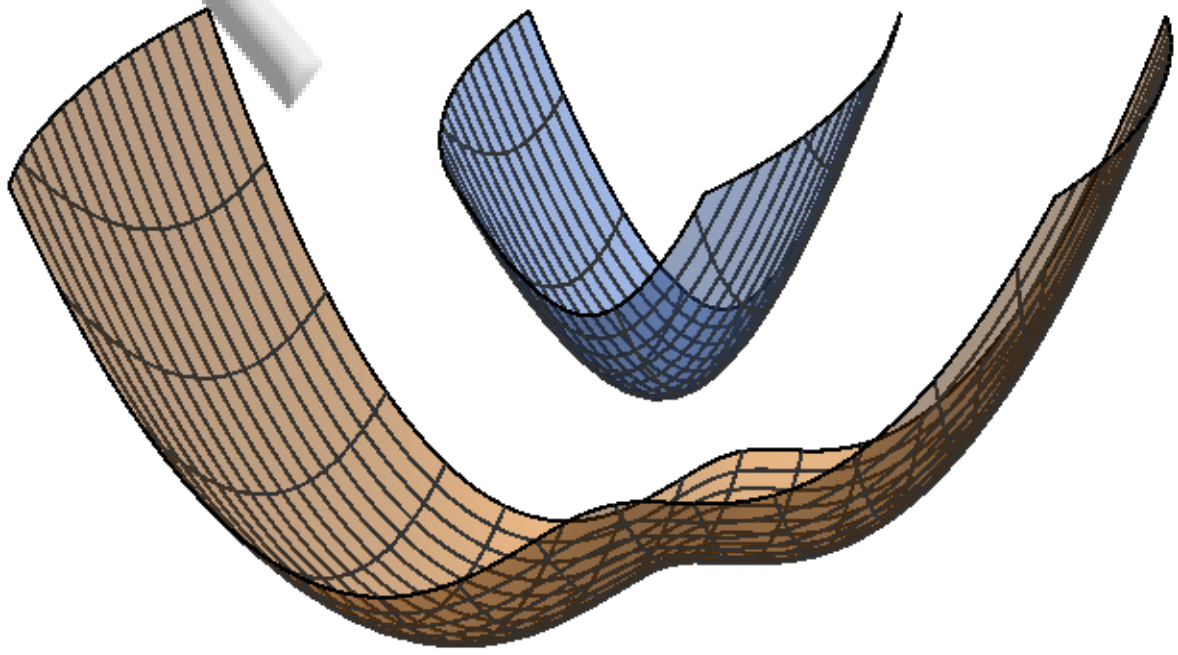

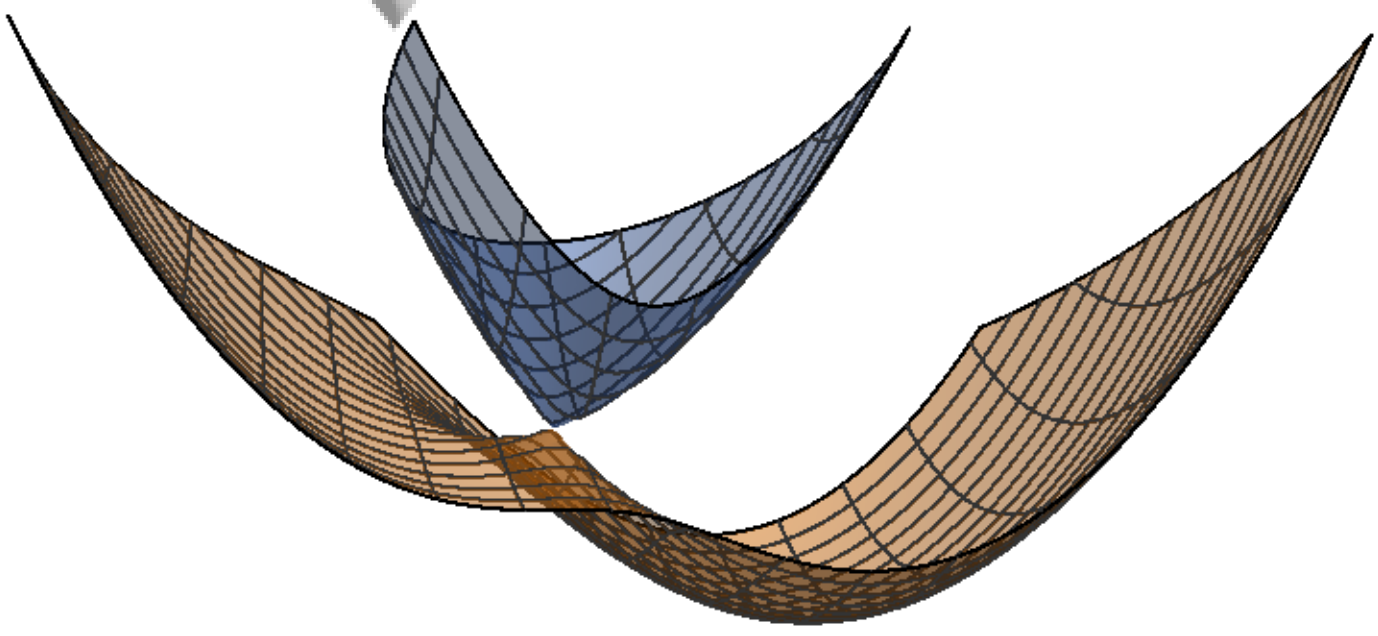

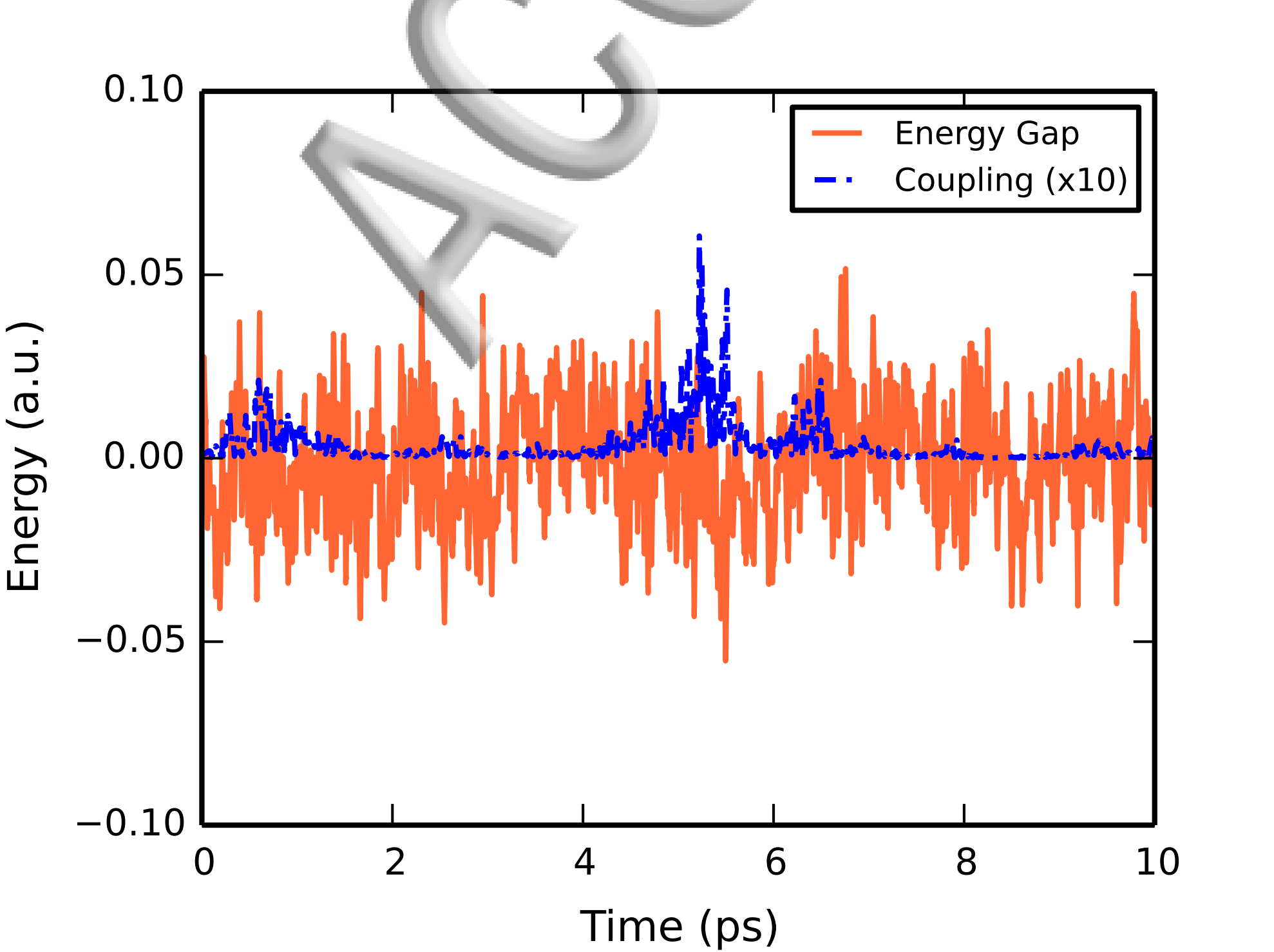
0.10
0.05
0.00
−0.05
−0.10
Energy (a.u.)
0
2
4
6
8
10
Time (ps)
Energy Gap
Coupling (x10)

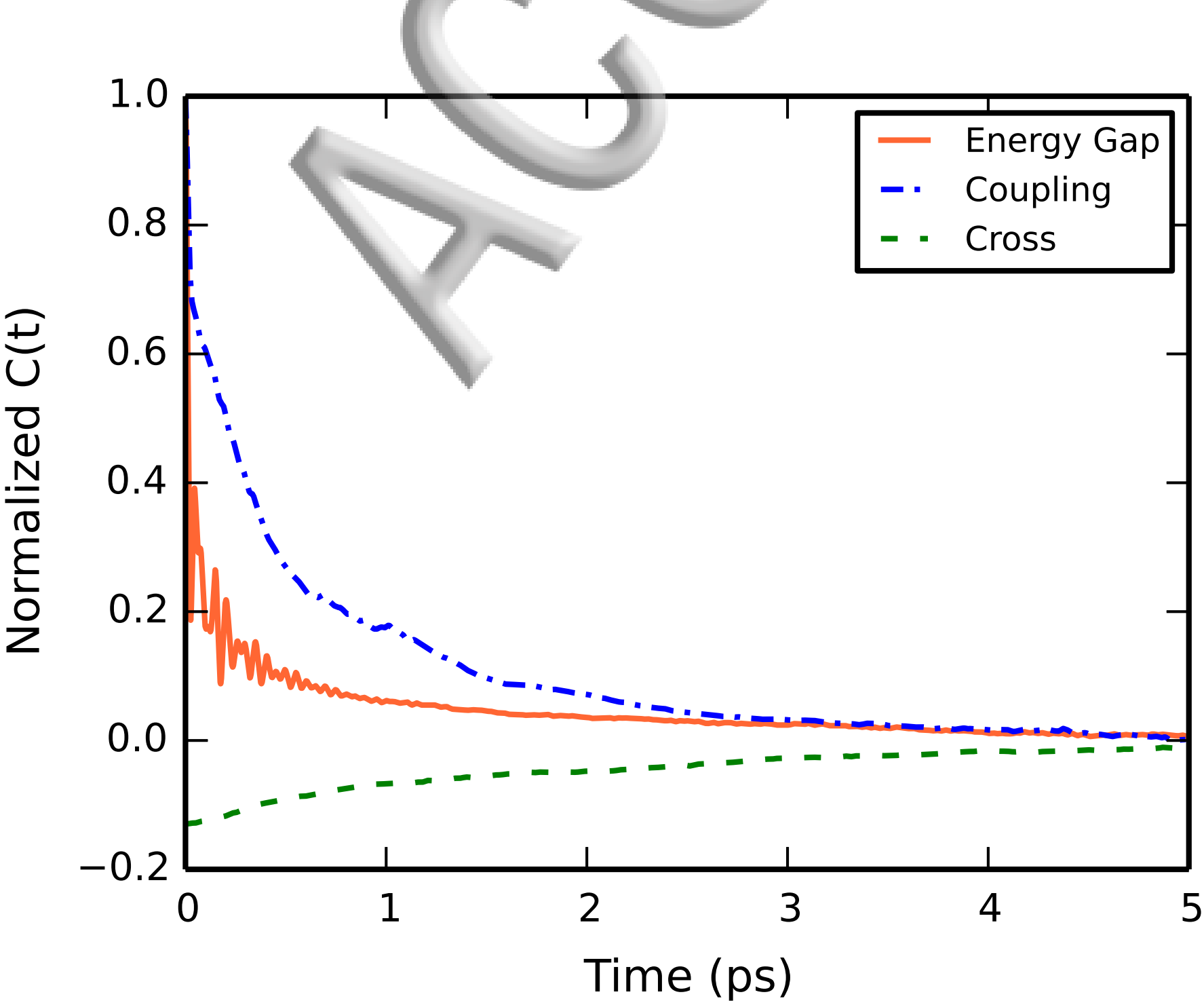
Energy Gap
Coupling
Cross
Normalized C(t)
Time (ps)
1.0
0.8
0.6
0.4
0.2
0.0
−0.2
0
1
2
3
4
5

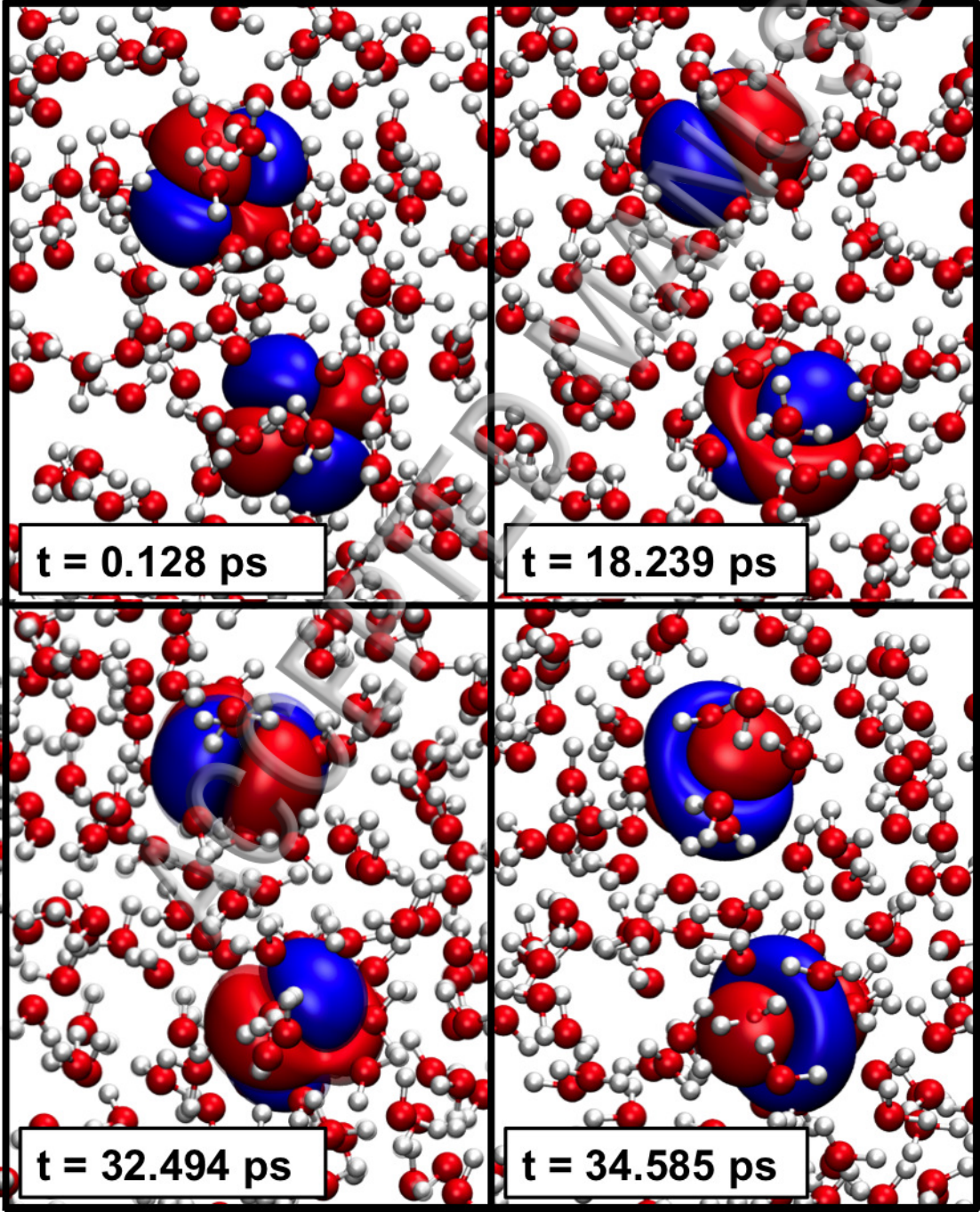
t = 0.128 ps
t = 18.239 ps
t = 32.494 ps
t = 34.585 ps

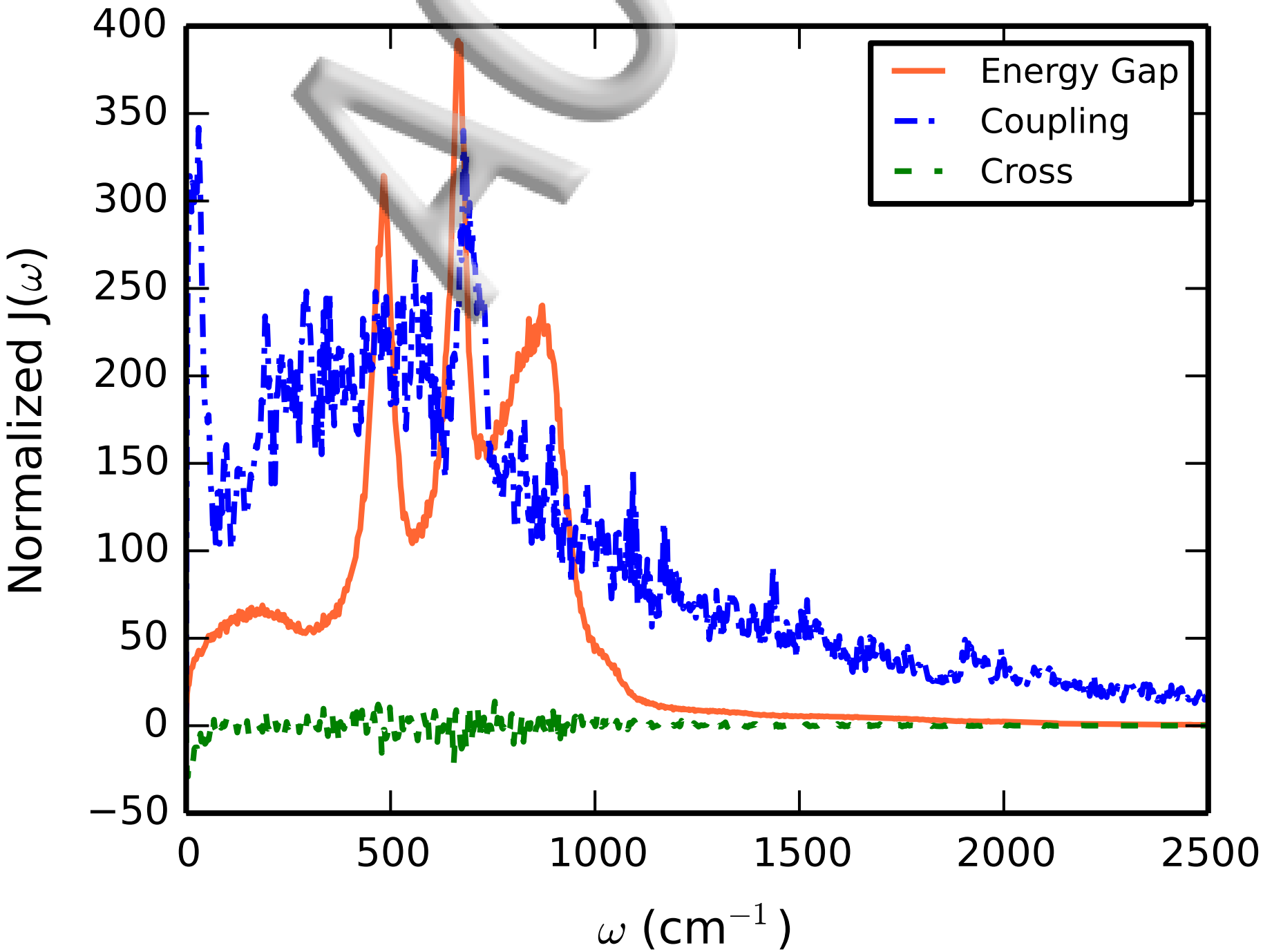
Energy Gap
Coupling
Cross
Normalized J(ω)
ω (cm⁻¹)
400
350
300
250
200
150
100
50
0
−50
0
500
1000
1500
2000
2500

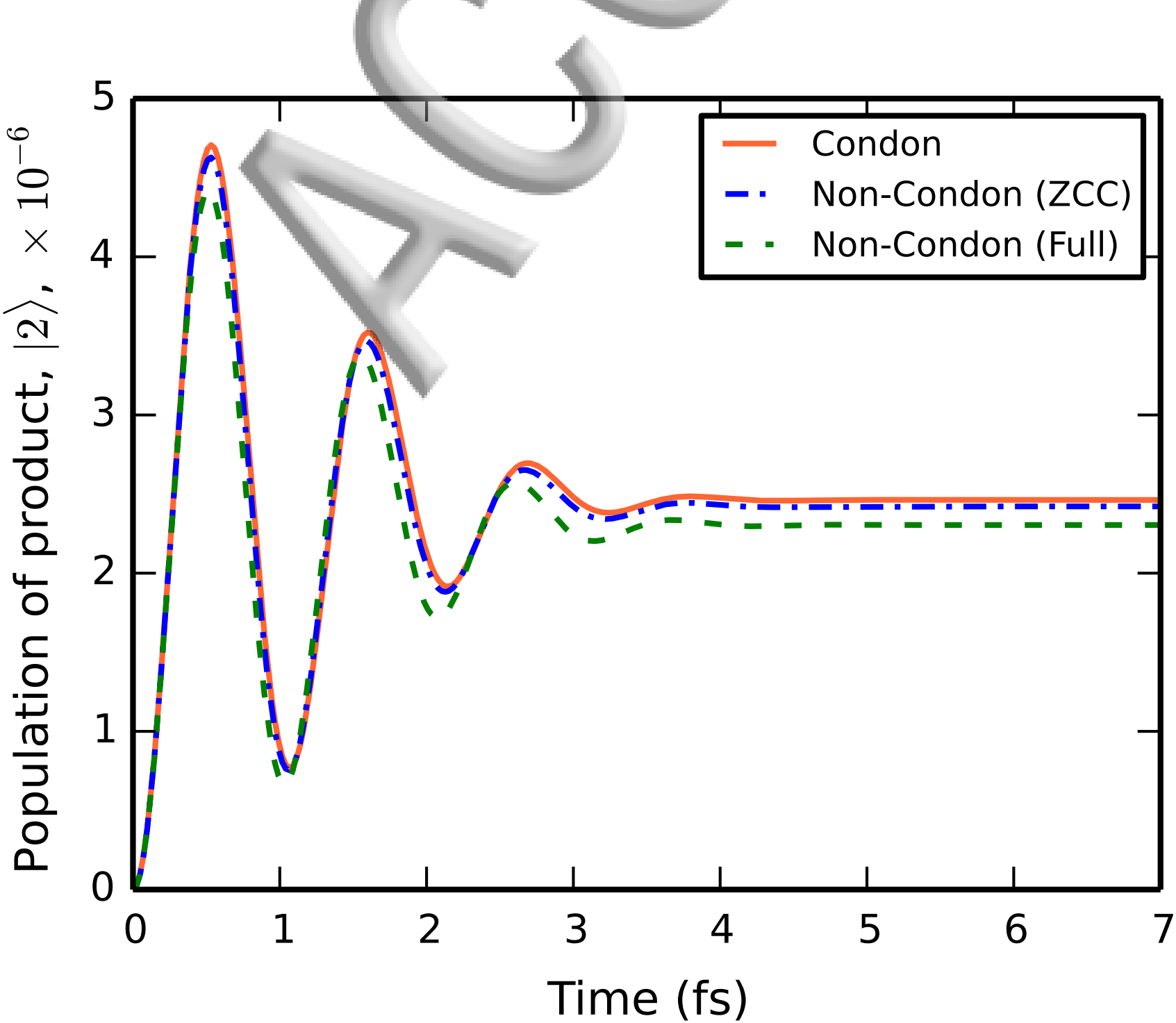
Condon
Non-Condon (ZCC)
Non-Condon (Full)
Population of product, $|2\rangle$, $\times 10^{-6}$
Time (fs)
0
1
2
3
4
5
6
7

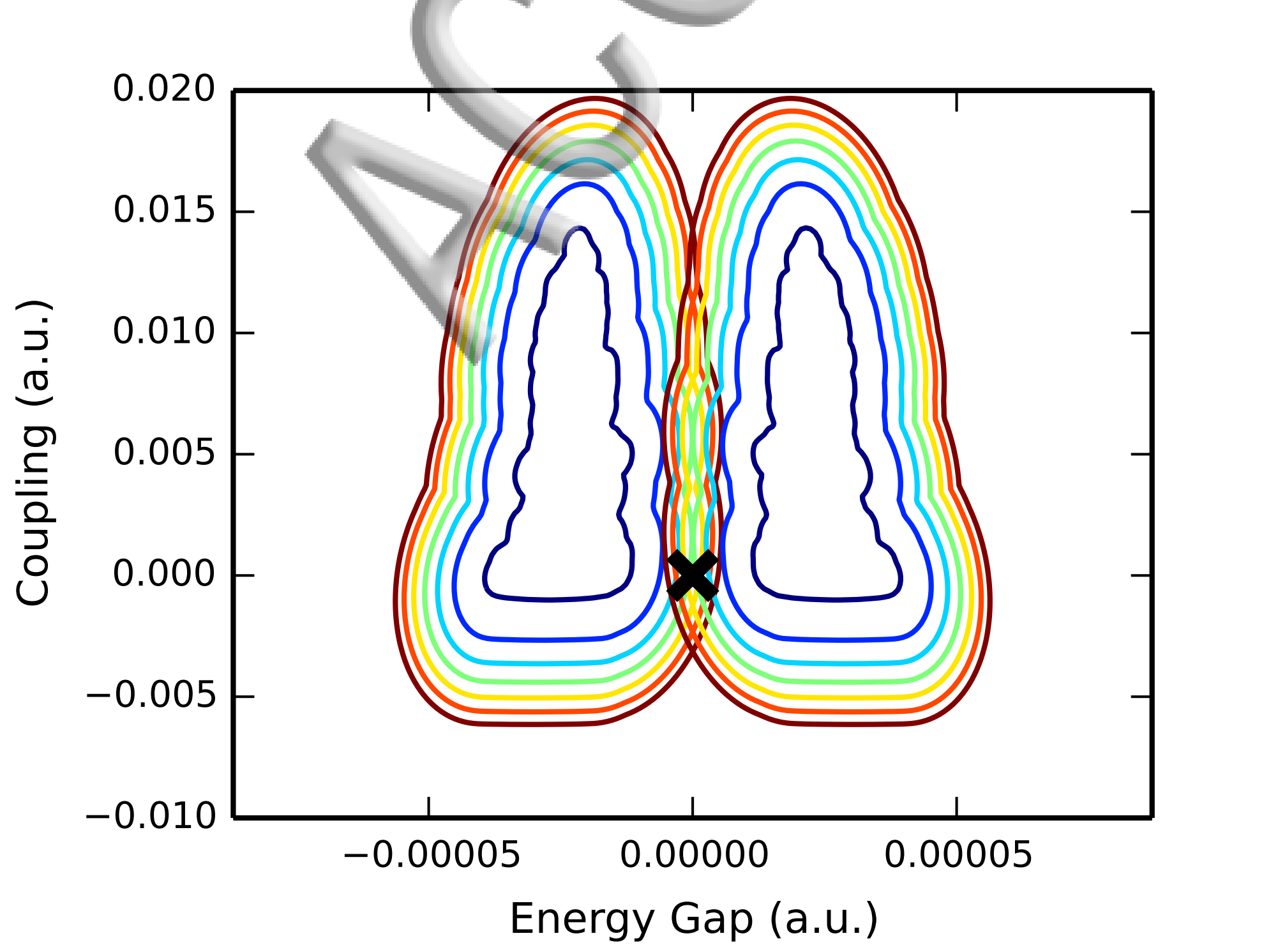
0.020
0.015
0.010
0.005
0.000
−0.005
−0.010
Coupling (a.u.)
−0.00005
0.00000
0.00005
Energy Gap (a.u.)

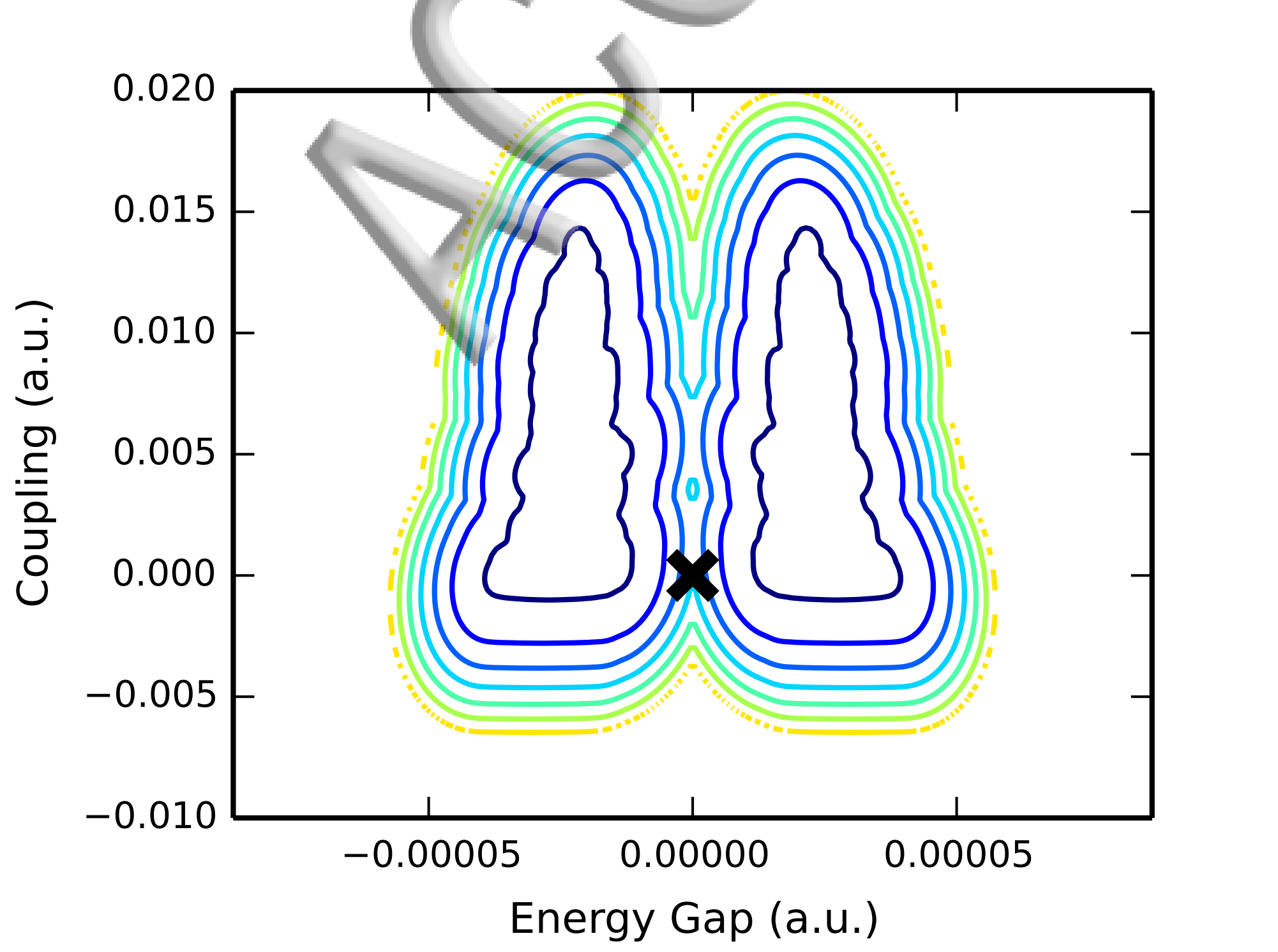
0.020
0.015
0.010
0.005
0.000
−0.005
−0.010
Coupling (a.u.)
−0.00005
0.00000
0.00005
Energy Gap (a.u.)

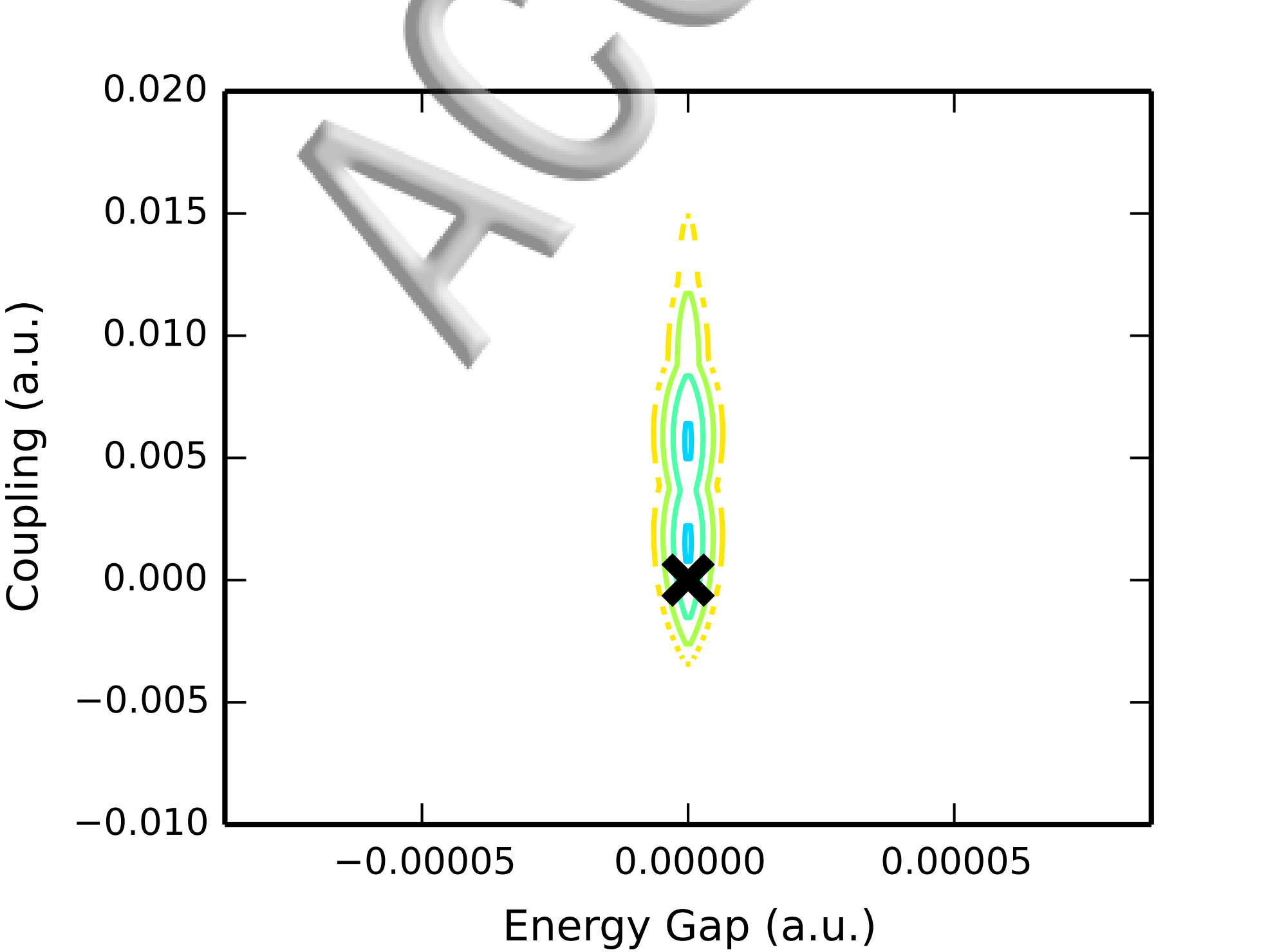
0.020
0.015
0.010
0.005
0.000
−0.005
−0.010
Coupling (a.u.)
−0.00005
0.00000
0.00005
Energy Gap (a.u.)

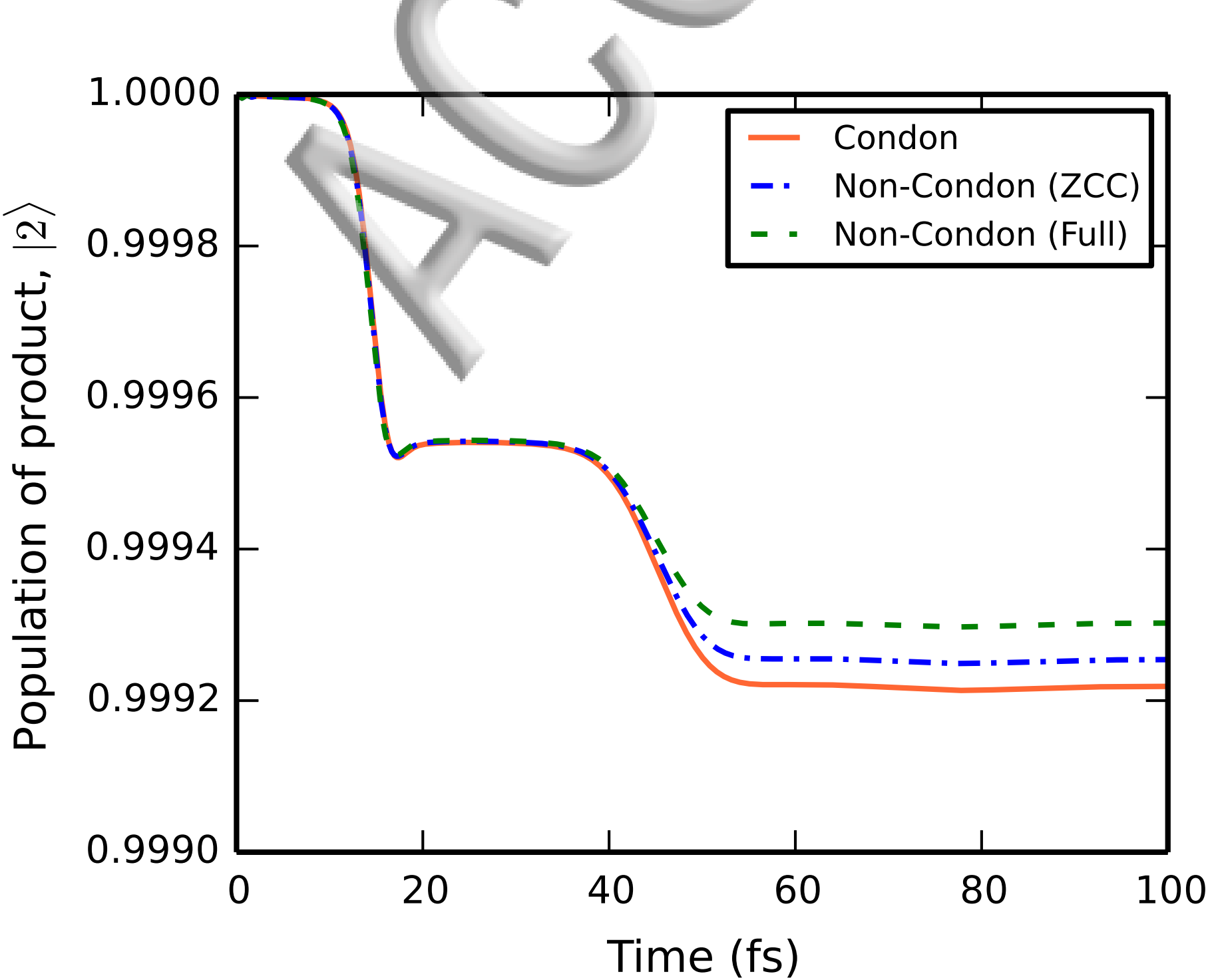
1.0000
0.9998
0.9996
0.9994
0.9992
0.9990
Population of product, $|2\rangle$
0
20
40
60
80
100
Time (fs)
Condon
Non-Condon (ZCC)
Non-Condon (Full)

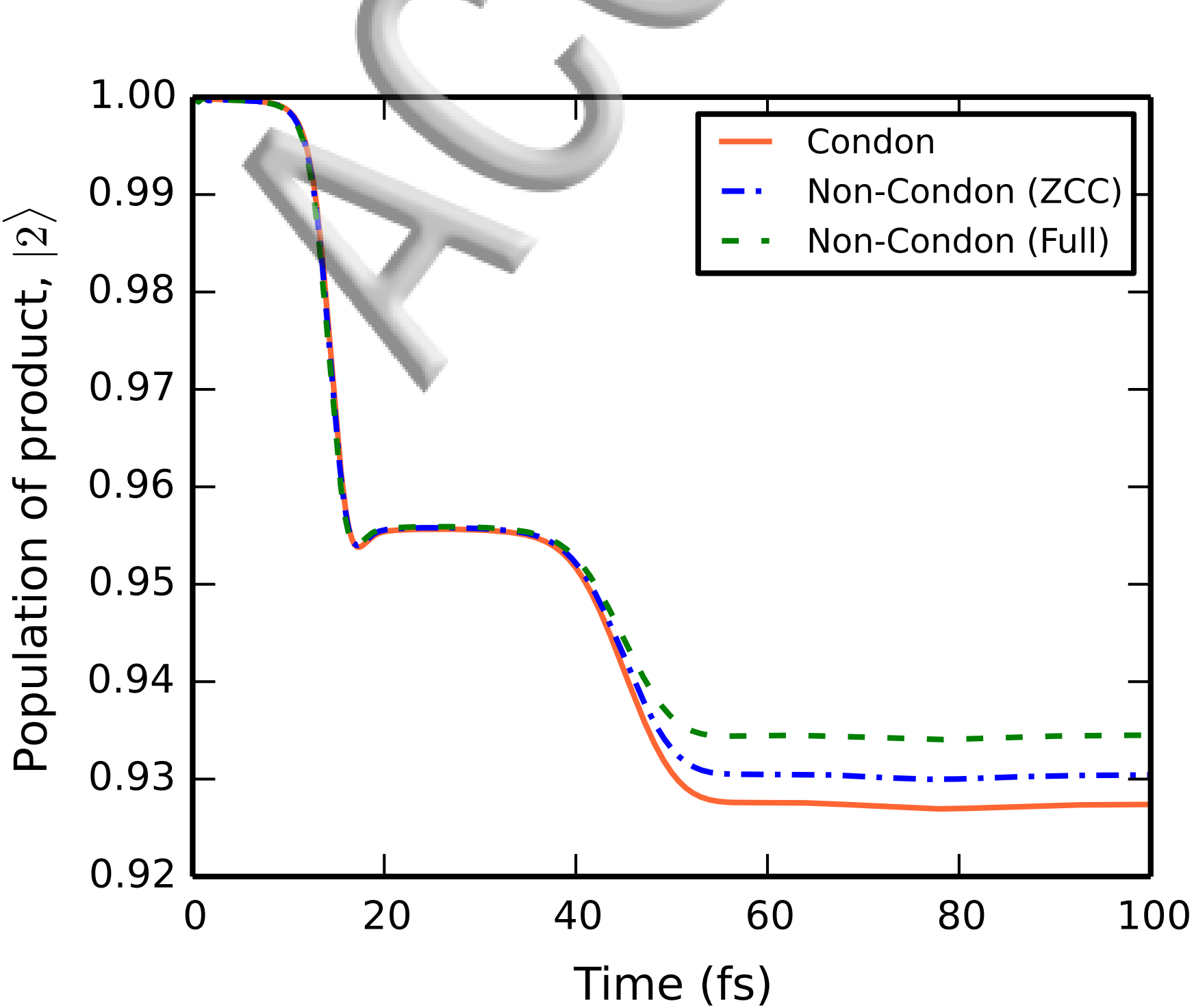
1.00
0.99
0.98
0.97
0.96
0.95
0.94
0.93
0.92
Population of product, $|2\rangle$
0
20
40
60
80
100
Time (fs)
Condon
Non-Condon (ZCC)
Non-Condon (Full)

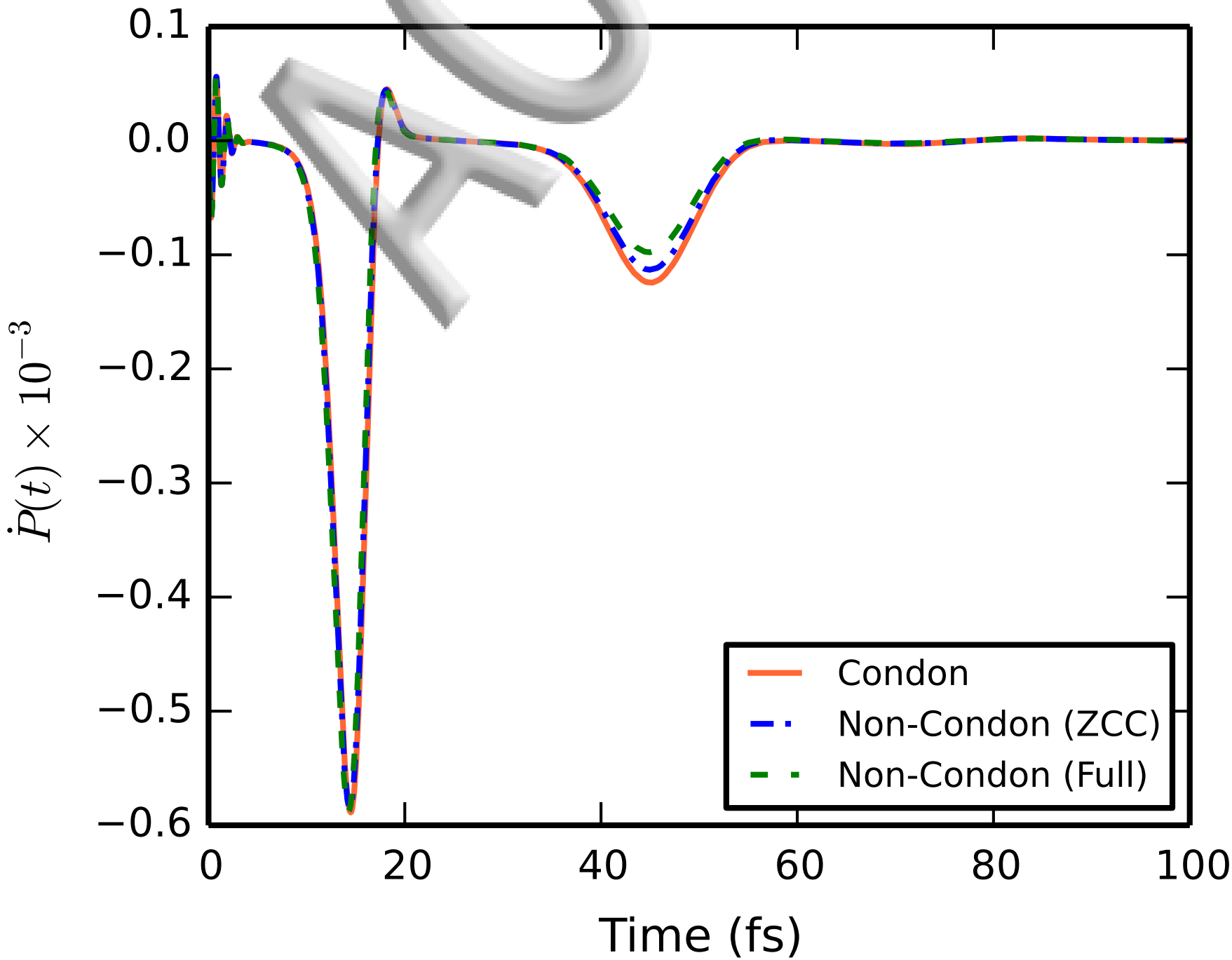
0.1
0.0
−0.1
−0.2
−0.3
−0.4
−0.5
−0.6
$\dot{P}(t) \times 10^{-3}$
0
20
40
60
80
100
Time (fs)
Condon
Non-Condon (ZCC)
Non-Condon (Full)